Analytical Solution of the Continuous Cellular Automaton for Anisotropic Etching

Miguel A. Gosálvez, Yan Xing, and Kazuo Sato

Abstract—The fabrication of micro- and nanoelectromechanical systems (MEMS/NEMS) is based on a wide variety of growth and etching technologies sequentially applied throughout process flows which may involve a dozen or more steps, their realistic simulation having become an essential part of the overall design. By focusing in the simulation of anisotropic etching as a complex example of microfabrication, in this paper, we show how to solve analytically the time evolution of the continuous cellular automaton method, thus providing a particularly suitable choice for the realization of realistic simulations for MEMS and NEMS applications. This paper presents a complete theoretical derivation of the analytical solution based on geometrical and kinetic aspects of step flow on any surface, including a new classification of the surface sites based on a mean-field treatment of the propagation of the steps. The results of the corresponding simulations are in good agreement with the experiments. The study can be seen as an example of a general procedure that is applicable to other interface propagation problems. **[2007-0167]**

Index Terms—Anisotropic etching, cellular automata (CA), simulation, step flow, surface processing.

I. INTRODUCTION

ANISOTROPIC wet chemical etching of crystalline silicon is a popular process for the fabrication of micro- and nanoelectromechanical systems (MEMS and NEMS). Although alternative technologies such as deep reactive ion etching (DRIE) have penetrated into the territories that are once exclusive of wet etching, the higher costs and, particularly, the limitations for batch processing using DRIE still make chemical etching the most affordable method for the reliable production of 3-D structures with multipurpose functionalities.

In spite of its wide use, the simulation of etching for MEMS applications has been so far a partial success only. One has to distinguish between two types of simulations: 1) those aiming at the prediction of the propagation of the etch front in engineering applications, often involving the combination of etching with other micromachining techniques, and 2) those targeting at the understanding of the process at the atomistic scale, including the description of a large variety of etched surface morphologies. Generally, the engineering applications have been dominated by the so-called geometrical simulators [1]–[4], where the etch front is described as a collection of planes (or facets) propagating along their normals according to the measured etch rates [5], [6]. Although these simulators have described successfully the propagation of the etch front in complicated geometries, their major drawback is the need of a full orientation-dependent etch rate database, such as ODETTE [6]. The larger the number of measured etch rates for different surface orientations, the more accurate the simulations become. The fact that so many etch rates are needed reminds of a "brute force" approach. Although interpolation has been successfully used between similar etching conditions, in practice, simulating the process under new etching conditions becomes a challenge requiring the measurement of the complete set of etch rates.

On the other hand, the atomistic simulators based on Monte Carlo (MC) and cellular automata (CA) methods have been successfully used for the understanding of the etching anisotropy as well as for explaining a wide variety of morphologic features originating from the process. In particular, the MC methods have shown that the relative stability of certain surface sites can have dramatic effects on the morphology and that diffusion transport and micromasking have a larger role than originally anticipated, leading to the formation of step bunches, pyramidal and trapezoidal hillocks, zigzag structures, and polygonal steps [7]–[10]. Most importantly, the use of these methods has provided a clearer picture of etching as a step-flow process [11]. In spite of this overall success, the MC methods have not been able to describe satisfactorily the propagation of the etching front for engineering applications, except with limited success [12].

In this respect, the CA simulators [13]–[16] have performed better, although also with limitations in spite of the accumulated tradition [17], [18]. Recently, Zhou *et al.* [19], [20] have presented a surface-site indexing scheme based on counting the numbers of interior and surface nearest neighbors ($1i$ and $1s$, respectively) and next nearest neighbors ($2i$ and $2s$) of the surface atoms, enabling more accurate CA simulations by providing better control over the fast etching planes. Although this suggests that the main reason for a traditionally limited success in the atomistic engineering simulations is an incomplete characterization of the surface sites involved in etching, this paper stresses the perspective that it is equally important (if not more) to incorporate the step-flow aspects of the process directly into

M. A. Gosálvez was with the Department of Micro-Nano Systems Engineering, Nagoya University, Nagoya 464-8603, Japan. He is now with the Laboratory of Physics, Helsinki University of Technology, 02015 Espoo, Finland (e-mail: mag@fyslab.hut.fi).

Y. Xing was with the Department of Micro-Nano Systems Engineering, Nagoya University, Nagoya 464-8603, Japan. He is now with the Department of Mechanical Engineering, Southeast University, Nanjing 211189, China (e-mail: xingyan@seu.edu.cn).

K. Sato is with the Department of Micro-Nano Systems Engineering, Nagoya University, Nagoya 464-8603, Japan (e-mail: sato@mech.nagoya-u.ac.jp).

the CA simulation. When doing so, a complete understanding of the mechanism can be achieved, thus enabling the analytical solution of the dependence of the surface etch rates on the atomistic reaction rates.

The importance of the step-flow aspects of anisotropic etching is due to the high stability of the (111) crystallographic surface against etching, which promotes the formation of (111) terraces separated by steps. Anisotropic etching consists essentially on the removal of atoms from the steps, giving rise to step propagation. This step-flow nature was established in the early 1990s through a combination of *in situ* STM observations [21], theoretical analogies between etching and growth [22], and microscopy and spectroscopy experiments [23]–[25]. The idea of step flow matured during the late 1990s, resulting in the development of atomistic etching simulators that use step propagation in one way or another [7], [12], [26], [28], [29]. Earlier MC [30]–[33] and CA [17], [18] simulators did not recognize the importance of step flow. Even today, the presentation and discussion of CA models for the simulation of anisotropic etching [15], [16] typically disregard the role of step flow. In this paper, we show how the step-flow aspects of etching are incorporated into the otherwise geometrical evolution provided by a CA simulation approach.

The step-flow analysis presented in this paper has been possible due to the explicit development of a tool for the visualization of step propagation on any generic surface using the CA method. The tool is a user-oriented simulator which we refer to as "VisualTAPAS." It allows inspecting the geometry and the surface-site configurations for any $\{hkl\}$ surface orientation as well as monitoring the evolution of the surface according to a number of methods, including the CA. In addition to the pedagogical value, the tool also allows the simulation of anisotropic and DRIE etching for rather complicated MEMS systems. The simulator can be freely downloaded from the web [34]. VisualTAPAS stands for "Visual Three-dimensional Anisotropic Processing at All Scales."

This paper focuses on the detailed analysis of the geometry and the kinetics of step flow on any generic surface orientation. As a result of the analysis, a consistent classification of the surface sites is introduced, which enables a robust theoretical description of the analytical form of the etch rate when the process is simulated with a CA. We use a continuous CA (CCA), which is a generalization introduced by Zhu and Liu [14], [15] for the CA method. In the CCA method, the silicon substrate is described as a collection of sites which can be fully or partially occupied by atoms, and the propagation of the surface is described as the overall result of gradually decreasing the occupation of the sites according to the site-dependent removal rates of the atoms.

This paper focuses on the CA approach partly because this type of method is strongly emerging not only for growth and etching but also for fluid flow (diffusion limited), reacting systems in chemistry, pattern formation, development of organisms and ecosystems, traffic design and analysis, or even urban growth. The CA method can reliably include both wet and DRIE etching (as well as different growth technologies) in the simulation tools for the design of MEMS and NEMS. In comparison to the more traditional geometrical simulators

[4], [5], the atomistic modeling provides a natural link between surface processing, bulk micromachining [13], [19], and structure analysis [35], [36] through the atomistic discretization of the system. It also provides the possibility to understand the system evolution as the result of a characteristic step-flow process, gaining valuable insight as compared to the propagation of planes in the geometrical approach.

The exact solutions for the etch rates make the realization of accurate simulations of anisotropic etching possible. This is achieved through a fitting procedure in which the atomistic removal rates appearing in the analytical expressions are solved in terms of the experimental values of the etch rates for several surface orientations used as inputs. The comparison of the results from the simulations to available experiments demonstrates the validity of the theoretical analysis. This reduces the amount of input experimental etch rates necessary for simulating the process accurately.

This paper has been organized into three major sections in addition to this Introduction. Sections II and III constitute the core of the study and may become rather technical as the purpose of this paper is to provide a self-contained analysis of all the features that need to be considered in order to derive the analytical expressions. In Section II, we introduce new notation and a new systematic classification of the surface sites based on the concepts of restriction and edging. These concepts allow us to differentiate between sites that are close to the steps—both on the upper and lower terraces—and sites that are far. Together with the fundamental idea of step flow, the two concepts are a key element without which the analytical solution of the etch rates in Section III would be an impossible task. In order to make the classification of the sites more comprehensive, we include a detailed analysis of the underlying crystallographic geometries in Sections II-A–C, showing that many of the surfaces can be themselves classified into three families which actually share many aspects, most importantly, restriction and edging. In Section IV, we present the fitting procedure through which the atomistic rates for the different atoms can be obtained, and we compare the results of several simulations to the experiments, showing very good agreement. In Sections V and VI, we present a discussion of the merits and limitations of our approach and the conclusions of this paper, respectively.

II. ORIENTATION-DEPENDENT GEOMETRY AND CLASSIFICATION OF THE SURFACE SITES

As mentioned already, wet etching is essentially a step-flow process [11]. Depending on the nature of the steps, there are differences in the details of the step propagation, and it becomes useful to classify the surfaces according to the steps appearing on them. In this section, the geometry of the different surface orientations is analyzed from the perspective of step flow. In turn, this makes the derivation of the etch rates for arbitrary orientations easier (Section III).

In this paper, we distinguish between five types of surfaces, namely, the M, L, H, V, and K surfaces. Although the full details of this classification are presented in the succeeding discussions, a quick reason for the five surface types is as follows. On misaligned (111) surfaces, traditionally, one finds

two types of steps: the monohydride (M) and the dihydride (D) terminated steps, with the peculiarity that the latter can appear as two different realizations: the horizontal (H) and the vertical (V) step dihydrides. As a result, one can distinguish between M, H, and V misaligned (111) surfaces. In addition, when a full row of M step atoms is removed, a complete row of singly bonded trihydride-terminated atoms is left behind. We refer to these atoms as lollies and denote them with the symbol L (more about this name later). The corresponding L surfaces are essentially equivalent to the M surfaces, except for the nature of the sites located right at the step. This is similar to the H and V surfaces, which are equivalent except precisely at the steps. In addition to these four surfaces, we need to include misaligned (110) surfaces characterized by displaying steps made of kink sites (K). This gives a total of five step types and, correspondingly, five kinds of surfaces. Due to the strong relation between the M and L surfaces and the H and V surfaces, one can eventually distinguish between three main surface families: the M, D, and K families. The M family contains M and L realizations, and the D family contains H and V realizations. The K family has a single realization only.

In spite of the technical details, one should keep in mind that the purpose of this section is to describe the geometrical similarities between the three main surface families. These similarities justify the definition of the concepts of restriction and edging, which provide a simple, yet powerful, means of classifying the numerous surface sites appearing during the step-flow-based propagation of the surfaces. The analogies between the three families are summarized in the value of the step-to-terrace ratio (to be introduced later), which is almost identical across the three families, as will be shown.

In addition to the geometrical aspects related to the step flow, the analysis that will be discussed later provides a useful background for understanding which experimental etch rates (i.e., from which orientations) are essential for the successful realization of a fitting procedure that allows performing accurate atomistic simulations of etching, as shown in Section IV. This is important in order to appreciate the significant reduction in the number of experimental etch rates that is necessary for simulating the process in comparison to the geometrical methods.

A. M Surface Family

The M family refers to vicinal (111) orientations whose ideal crystallographic cut displays monohydride sites located at the steps, as shown in Fig. 1(a) and (b). These step sites are traditionally denoted as step monohydrides (SMs) to differentiate them from the terrace monohydrides (TMs) appearing at the terrace regions [25]. As shown in Fig. 1(c) and (d), the M family contains the $(h+2 \ \ h+2 \ \ h)$ and $(h \ \ h \ \ 1)$ subfamilies, where h is an integer $h > 1$ and $h > 2$, respectively. The notation $(h+2 \ \ h+2 \ \ h)$ is subjected to division by a common multiplier of the resulting $(h \ \ k \ \ l)$ values.

The $(h+2 \ \ h+2 \ \ h)$ subfamily displays an increasing number of terrace sites as h is increased. It is simple to check that $(h+2 \ \ h+2 \ \ h)$ has exactly h TM sites per terrace area. For instance, the inspection in Fig. 1(c) shows that
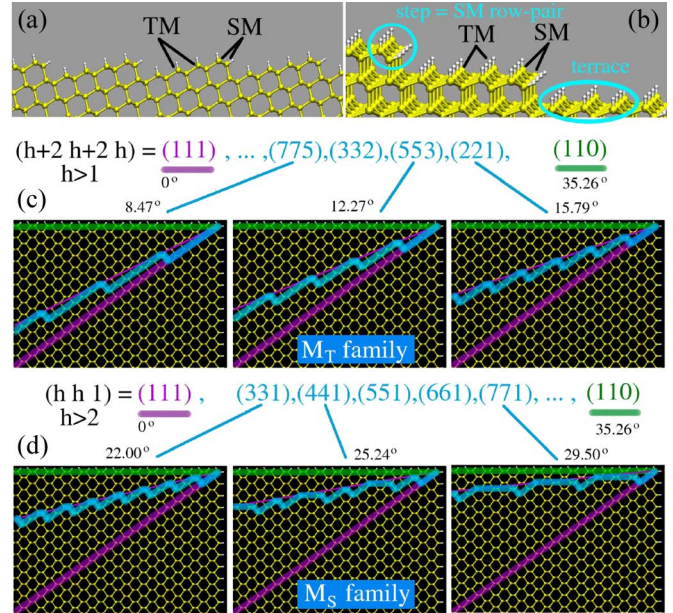

Fig. 1. Examples of surfaces from the M family. (a) Side view of (553) showing the TM and SM sites. (b) Close-up 3-D view of (553). (c) The M_T subfamily. (d) The M_S subfamily. Angles are with respect to (111).

$(442)(=(221))$ has two TMs in each terrace, (553) has three, $(664)(=(332))$ has four, etc. . . . If we define the step-to-terrace ratio ρ as the ratio of the number of step sites to the number of terrace sites, then we have $\rho = 2/h$. Here, the numerator 2 is due to the fact that every step is made of two rows of SM sites, as shown in Fig. 1(b). Due to this feature, we will refer to the SM steps as "SM row pairs."

In contrast, as h increases the $(h \ \ h \ \ 1)$ subfamily shows an increasing number of steps (i.e., SM row pairs) and a decreasing number of terraces, as shown in Fig. 1(d). In fact, in this whole family, each terrace has been reduced to a single TM row. As h increases, the structure of the surface displays a characteristic pattern that depends on whether h is even or odd. As an example, (331) shows one SM row pair for each TM row, whereas (441) shows a more complicated structure consisting of two SM row pairs, one TM row, one SM row pair, and one TM row. This structure forms a basic pattern that is repeated periodically. For simplicity, we may refer to this repeated structure as [2, 1, 1, 1]. If we now consider the (551) orientation, the repeated structure is [2, 1, 2, 1], i.e., two SM row pairs, one TM row, two SM row pairs, and one TM row. Similarly, the repeated block becomes [3, 1, 2, 1] for (661) and [3, 1, 3, 1] for (771), as explicitly shown in Fig. 1(d). Thus, for the generic $(h \ \ h \ \ 1)$ surface, the repeated block is $[h/2, 1, h/2 - 1, 1]$ if h is even and $[(h-1)/2, 1, (h-1)/2, 1]$ if h is odd. In spite of this difference between the even and odd indices, the step-to-terrace ratio for the whole $(h \ \ h \ \ 1)$ subfamily is calculated simply as $\rho = h - 1$. For the even case, one has $\rho = (2(h/2) + 2(h/2 - 1))/(1 + 1) = h - 1$. For the odd case, $\rho = (2(h - 1)/2 + 2(h - 1)/2)/(1 + 1) = h - 1$.

Since the most essential difference between the $(h+2 \ \ h+2 \ \ h)$ and $(h \ \ h \ \ 1)$ subfamilies is the relative number of terrace and step sites, we will refer to them as the terrace-rich M surfaces (or, simply, the M_T family) and the
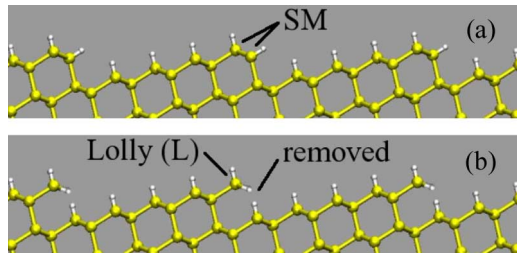
Fig. 2. Definition of the lolly sites giving rise to the L family, a small variation of the M family. (a) and (b) M and L realizations of (553), respectively.

step-rich M surfaces (or M_S family), respectively. This feature is reflected in the value of the step-to-terrace ratio, which is less than one for the former ($\rho = 2/h < 1$) and larger than one for the latter ($\rho = h - 1 > 1$).

Note that (331) can, in principle, be considered as an element of both the M_T and M_S families. However, it unambiguously belongs only to the $(h \quad h \quad 1)$ family (M_S) since the terrace regions contain a single TM row, which is a prevailing characteristic of the rest of the M_S orientations. This is in contrast to the M_T surfaces, which have two or more TM rows at the terrace areas. The number of TM rows in the terrace regions is important because the TM rows located at the edges of the region (i.e., in close proximity to the steps) can be classified as different sites from those at the center region, as will be explained in detail in Section II-D. This makes the terraces of the M_T family behave in a different manner from the terraces of the M_S orientations.

When one of the SM rows in the SM row pair is removed, as shown in Fig. 2, a complete row of singly bonded trihydride sites is left behind. We refer to these sites as lollies or lollipops (L). This type of site is described in growth as an "adatom," particularly when the singly bonded atom occurs on a terrace. Since, in etching, we remove the atoms instead of adding them, we prefer the use of the term "lolly," which, in our opinion, is quite descriptive of the corresponding geometry. This gives rise to the L surface family, which is equivalent in every respect to the M family, except for the fact that the steps are single L rows instead of SM row pairs and the terraces in the L_T subfamily $(h+2 \quad h+2 \quad h)$ have $h+1$ TM rows instead of h for the M_T subfamily.

B. D Surface Family

The D family contains surface orientations whose ideal crystallographic cut displays dihydride sites located at the steps, as shown in Fig. 3(a)–(d). Traditionally, there are two types of step dihydrides, namely, the horizontal and the vertical step dihydrides (HSD and VSD, respectively) [25]. The difference depends on whether the dihydride unit containing the silicon atom and the two hydrogens lies on a plane that is (almost) horizontal or (almost) vertical with respect to the terrace plane, which is assumed horizontal [cf. Fig. 3(b) and (d)]. During etching, particularly using the CCA method, the VSD sites appear after the removal of the HSDs, and reversely, the HSDs appear after removing the VSDs. Accordingly, one may consider that the D family has two alternative realizations, the H and V
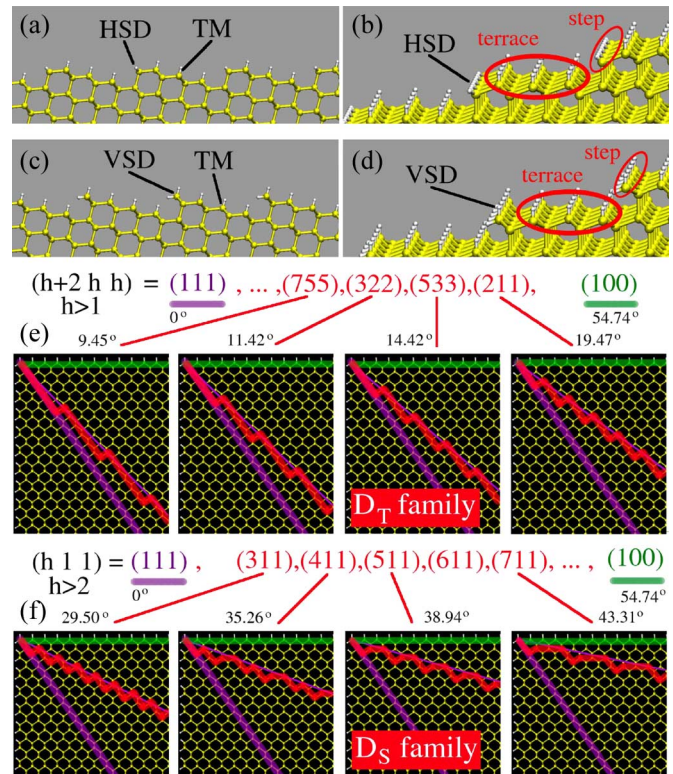

Fig. 3. Examples of surfaces from the D family. (a)–(b) Side and 3-D views of (533) showing the HSD sites. (c)–(d) Side and 3-D views displaying the VSD sites. (e) The D_T subfamily. (f) The D_S subfamily. Angles are with respect to (111).

families, equivalent in every respect except for the nature of the sites located exactly at the steps. This is similar to the case of the M and L realizations of the M family.

As in the case of the M family, the D family also contains two subfamilies, namely, the $(h+2 \quad h \quad h)$ and the $(h \quad 1 \quad 1)$ surfaces, where $h > 1$ and $h > 2$, respectively. The two subfamilies differ in the relative number of steps and terraces, with the former being terrace-rich (and, thus, referred here as the D_T family) and the latter being step-rich (and, thus, referred here as the D_S family).

The step-to-terrace ratio for the D_T family $(h+2 \quad h \quad h)$ is $\rho = 1/h$ since, in this case, there is only a single HSD row per step (in comparison, the M_T surfaces have two SM rows per step) and there are h TM sites per terrace area, as a simple inspection in Fig. 3(e) shows. As an example, (755) has five TMs in each terrace, $(644)(= (322))$ has four, (533) has three, etc.... In a similar manner, the step-to-terrace ratio for the D_S subfamily $(h \quad 1 \quad 1)$ is calculated as $\rho = (h-1)/2$. This is very similar to the case of the M_S orientations, where $\rho = h - 1$, the difference being the number of rows making the step in each case (two for the M family and one for the D family). As in the case of the M_S surfaces, the odd and even D_S orientations display a different structure, described as $[h/2, 1, h/2 - 1, 1]$ if h is even and $[(h-1)/2, 1, (h-1)/2, 1]$ if h is odd. If h is even, one has $\rho = (h/2 + (h/2 - 1))/(1 + 1) = (h-1)/2$. If h is odd, $\rho = ((h-1)/2 + (h-1)/2)/(1 + 1) = (h-1)/2$. Thus, (311) has 1 step site per terrace site, (411) has $3/2 = 1.5$, (511) has $4/2 = 2$, and so on. Note that the step-to-terrace ratio
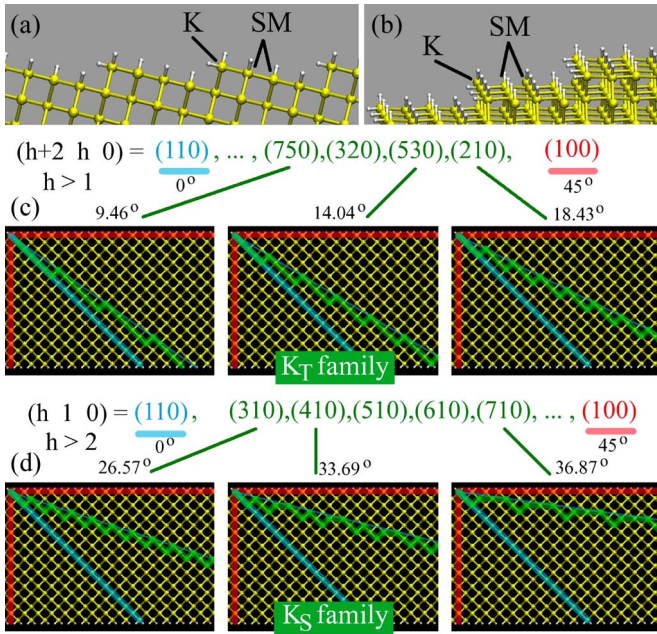
Fig. 4. Examples of surfaces from the K family. (a), (b) Side and 3-D views of (530). (c) The K_T subfamily. (d) The K_S subfamily. Angles are with respect to (110).

for the D_T and D_S subfamilies is independent of whether we consider HSD or VSD terminated surfaces.

As in the case of (331) for the M family, (311) can, in principle, be considered as a representative of both the D_T and D_S surface families. However, as before, for the M family, the fact that the TM sites appear as a single row in the D_S family transforms them into a different site type than the TM sites observed in the D_T orientations. As a result, (311) is a member of the D_S family and not of the D_T family. This will be shown in detail in Section II-D.

C. K Surface Family

The previous division of vicinal (111) orientations into the M and D families is the result of a purely geometrical description of the corresponding crystallographic cuts. A similar characterization can be performed for vicinal (110) surfaces inclined toward (100). As shown in Fig. 4(a), in this case, the regions appearing as "terraces" are actually made up of SM sites (in comparison to the TM sites appearing on the real (111) terraces), and the "steps" are made up of kink (K) sites (instead of pure step sites as in the previous families). Thus, we define the K family as composed by (110) stepped surfaces whose ideal crystallographic cut displays K sites at the "steps" and SM sites at the "terraces." We stress that, for the K family, the terms "steps" and "terraces" are only used as an extension of the analysis of vicinal (111) planes.

As in the case of the M and D families, the K family also contains two subfamilies, namely, $(h + 2 \quad h \quad 0)$ and $(h \quad 1 \quad 0)$, where $h > 1$ and $h > 2$, respectively. The two subfamilies differ in the relative number of K and SM sites, with the former family being terrace-rich (and, thus, referred here as the K_T family) and the latter being step-rich (and, thus, referred here as the K_S family).

The step-to-terrace ratio for the $(h + 2 \quad h \quad 0)$ or K_T subfamily is $\rho = 1/h$ since there are h SM rows per terrace and one single K row per step. For the $(h \quad 1 \quad 0)$ or K_S family, one has $\rho = (h - 1)/2$, which is similar to the case of the D_S and M_S families. This is due to the fact that identical alternations between groups of steps and single-row terraces occur in the three step-rich families (M_S, D_S, and K_S), resulting in completely equivalent structures for the even and odd h values across the three families.

As in the case of (331) for the M family and (311) for the D family, (310) can be considered as a representative of both the K_T and K_S subfamilies. However, because the SM sites appear as a single row in the terrace regions of the K_S family, they correspond to a different site type than the SM sites observed in the K_T orientations, explaining why (310) is a member of the K_S family and not of the K_T family.

Table I summarizes the most distinctive geometrical features of the M, D, and K families. The symmetry between the three families is notorious.

D. Edging and Restriction: Classification of the Surface Sites

The previous similarities between the M, D, and K families highlight the fact that the terrace width in all three families shrinks down gradually as we move away from (111) and (110), eventually becoming a single-row terrace once we enter the step-rich subfamilies (M_S, D_S, and K_S). In order to account for the orientation dependence of the etch rate, this change in the environment of the terrace sites (and, accordingly, of the other sites also) should be taken into consideration. The simplest way to do this is to recognize the different terrace sites as different site types. For instance, the sites located at the center of a wide terrace region can be considered to be different from those located near the steps. Following this idea, we define two additional site types or variants of the traditional terrace sites: the edge and restricted terrace sites.

"Restriction" refers to the situation where a step is close to the terrace site, thus restricting the amount of space around that site. This is schematically shown in Fig. 5(a), where restriction by M and H steps is highlighted in blue and red, respectively. The M-restricted terrace site is denoted as T^M, and the H-restricted terrace site is denoted as T^H, with the traditional TM sites at the center region of the terrace denoted simply as T. The M and H step sites correspond to the previously denoted SM and HSD sites according to the standard notation.

Restriction can also occur due to the proximity of V and L steps, as shown in red and blue in Fig. 5(b), respectively. The L-restricted and V-restricted terrace sites are denoted as T^L and T^V in Fig. 5(b). The V step sites correspond to the previously denoted VSD sites (standard notation).

In a similar manner, the term "edging" is used to describe a terrace site that is located at the edge of a terrace region in the proximity of a step. As an example, there are edge terrace sites at the M, H, V, and L steps, as shown in Fig. 5(a) and (b). The edge location is denoted using a subindex, in opposition to restriction, which uses a superindex. For instance, the edge terrace at the M step is denoted by T_M. Similarly, T_V describes the edge terrace at a V step.

TABLE I
MAIN SURFACE FAMILIES AND THEIR SUBFAMILIES. ρ IS THE STEP-TO-TERRACE RATIO (SEE TEXT).
X_{T} = TERRACE-RICH X SUBFAMILY. X_{S} = STEP-RICH X SUBFAMILY

Family	Sub-family	ρ	Comments
M (M and L realizations*)	M_{T} $(h+2\ h+2\ h),\ h>1$	$2/h$	A step contains two SM rows (row-pair) There are h TM sites per terrace region
	M_{S} $(h\ h\ 1),\ h>2$	$h-1$	h even: $[h/2,1,h/2\text{-}1,1]$-structure h odd: $[(h\text{-}1)/2,1,(h\text{-}1)/2,1]$-structure
D (H and V realizations)	D_{T} $(h+2\ h\ h),\ h>1$	$1/h$	A step contains only one HSD or VSD row There are h TM sites per terrace region
	D_{S} $(h\ 1\ 1),\ h>2$	$(h\text{-}1)/2$	h even: $[h/2,1,h/2\text{-}1,1]$-structure h odd: $[(h\text{-}1)/2,1,(h\text{-}1)/2,1]$-structure
K	K_{T} $(h+2\ h\ 0),\ h>1$	$1/h$	A step contains only one K row There are h SM sites per terrace region
	K_{S} $(h\ 1\ 0),\ h>2$	$(h\text{-}1)/2$	h even: $[h/2,1,h/2\text{-}1,1]$-structure h odd: $[(h\text{-}1)/2,1,(h\text{-}1)/2,1]$-structure

(*)In the L realization, steps contain a single L row and there are $h+1$ TM sites per terrace region.
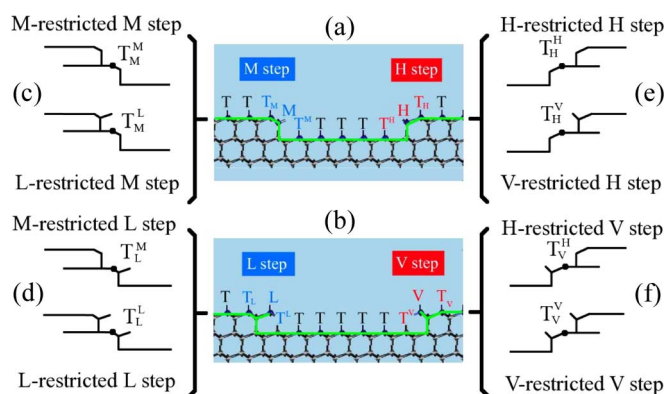

Fig. 5. Examples of edge and restricted terrace sites.

As a matter of fact, restriction can also occur for the edge sites, as schematically shown in Fig. 5(c)–(f). As an example, Fig. 5(f) shows that an H step can restrict the edge terrace at the V step, giving rise to the T_{V}^{H} sites. In a similar manner, the other restricted edge sites are denoted by the symbols T_{M}^{M}, T_{M}^{L}, T_{H}^{H}, T_{H}^{V}, and so on.

In addition to the use of the superindex- and/or subindex-based symbols to denote the sites, we find it useful to introduce an alternative acronym-based notation in which we use "XR-ETY" to refer to the T_{Y}^{X} sites. As an example, LR-ETM, which we read as "L-Restricted Edge Terrace at M," stands for T_{M}^{L}. Some additional examples are as follows: HR-T for T^{H}, read as "H-Restricted Terrace," when the terrace is restricted by the proximity of an H step; ETM for T_{M}, read as "Edge Terrace at M," when the terrace is at the edge of an M step; VR-ETH for T_{H}^{V}, read as "V-Restricted Edge Terrace at H," when the terrace is at the edge of an H step and is simultaneously restricted by a V step. The similarity between the two notations is apparent. The restricting agent goes to the front, and the edge location goes to the end of the acronym, whereas the symbol displays the restricting agent as a superindex, and the edge location as a subindex.

Fig. 6 shows an exhaustive collection of all the sites that can be identified through the arguments of restriction and/or edging in the M and D families. The figure describes how some of the site names change depending on the proximity of the restricting step. For instance, in Fig. 6(a), the T site changes into an MR-T

site when the restricting M step is close enough. Similarly, the ETM site changes into MR-ETM. In this case, the resulting site is identical to an M site, at least as far as the first and second neighbors of the two sites are concerned. Note that there are four different L sites in Fig. 6, namely, L(M), L(ETM), L(ETH), and L(T). These correspond to the lollies (or trihydrides) that are formed when removing a whole row (or layer) of M, ETM, ETH, and T sites, respectively, as shown in the fourth row of Fig. 6(b) and (d) (darker background color). We read the names of these lolly sites as follows: For L(M), we say "L of M," which is a shorter version of "Lolly of the M-site," i.e., the lolly site that is created by removing the M atoms. Similarly, we say "L of T" when reading L(T), "L of ETM" for L(ETM), and so on.

As one might guess, restriction and edging are not exclusive features of the M and D families, and one can consider similar spatial environments for the "terrace" sites in the proximity of the K "steps" (K family) and also for the dihydride-rich "terrace" regions in the D_{S} subfamily. In order to systematically characterize the additional configurations, we need to consider an extended set of basic sites, as shown in Table II. In this set, the D and A sites are added to the already introduced T, M, H, V, L, and K. As described in the table, the D sites appear on the (100) "terraces" of the D_{S} subfamily, which simply correspond to (100) crystallographic cuts [see Fig. 3(f)]. As in the case of the K family, the use of the term "terrace" to refer to these dihydride-rich flat regions is an abuse of terminology, but it helps in underlining the similarities between all the families. The A sites simply correspond to the monohydrides located at the steps between the dihydride-rich plateaus in the D_{S} subfamily [see Fig. 3(f)].

All the sites that can be identified for the K and D_{S} families have been gathered in Fig. 7. Here, we follow the same acronym notation as before, but substituting the "T" in XR-ETY by the corresponding "terrace" site (M or D). As an example, EMK denotes the "Edge Monohydride at K" and AR-EDA stands for "A-Restricted Edge Dihydride at A." Note that restriction by the K "steps" affects the "terrace" sites at two different distances, which we denote by using the KR(1) and KR(2) acronyms. For instance, the KR(2)-EMK site is an Edge Monohydride at K (EMK) restricted by the K step at the longer distance. We read it as "K-Restricted level 2 Edge Monohydride at K."
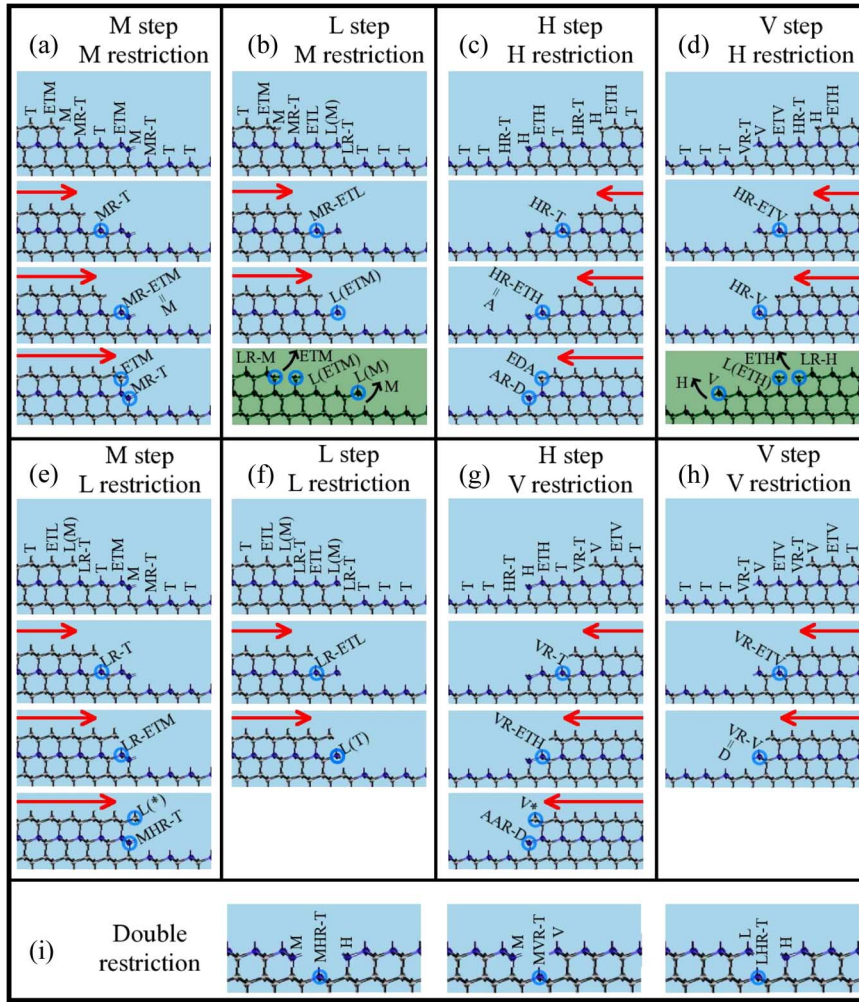
Fig. 6. Examples of sites.

TABLE II
BASIC SURFACE SITES

Symbol	Name	Std	Where is it found?
T	Terrace monohydride	TM	(111)-terraces
M	step Monohydride	SM	(110)-'terraces' and
			M-steps in M_T-family
H	Horizontal step dihydride	HSD	H-steps in D_T-family
V	Vertical step dihydride	VSD	V-steps in D_T-family
K	Kink	-	K-'steps' in K_T-family
D	Dihydride	-	(100)-'terraces'
A	Another monohydride	-	A-'steps' in D_S-family
L	Lolly	-	Any singly-bonded trihydride site

We have gathered all the surface sites in Table III, showing both the corresponding symbols and acronyms. The symbols are a particularly compact manner to refer to the sites as far as one remembers that the superindex denotes restriction and that the subindex corresponds to the edge location. In this respect, the acronyms are more advantageous, as the incorporation of the letters R and E reminds one on how to read them. This comes at the expense of a less compact representation. In addition, Table III includes a column labeled "Std" for the traditional (or standard) names, which are available only for a few sites, and a final column showing in which figure each site
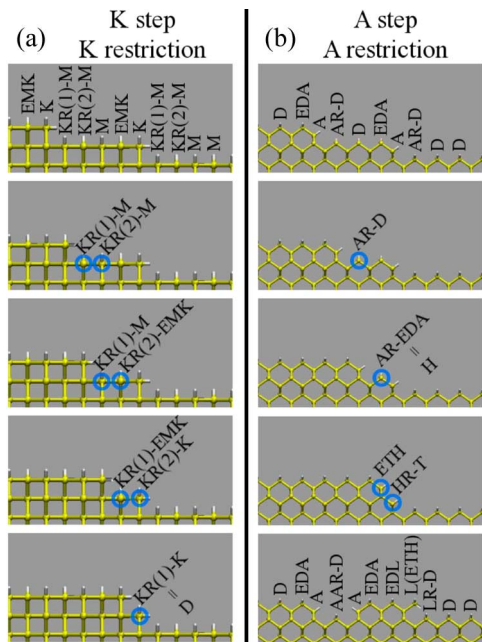
Fig. 7. Examples of sites.

TABLE III
CLASSIFICATION OF SITES ACCORDING TO RESTRICTION AND EDGING FOR STEP FLOW

#	Symbol	Acronym	Std	(n_1,n_2)	(n_1,n_2^d,n_2^i)	$(n_1^s,n_1^b,n_2^s,n_2^b)$	Figure
1	$T^{L,H}$	LHR-T	-	(3,11)	(3,9,2)	(0,3,4,7)	6(i)
2	T^L	LR-T	-	(3,11)	(3,9,2)	(0,3,6,5)	6(b,e,f)
3	$T^{M,V}$	MVR-T	-	(3,10)	(3,9,1)	(0,3,3,7)	6(i)
4	T^V	VR-T	-	(3,10)	(3,9,1)	(0,3,5,5)	6(d,g,h)
5	$T^{M,H}$	MHR-T	-	(3,9)	(3,9,0)	(0,3,2,7)	6(i)
6	T^M or T^H	MR-T or HR-T	-	(3,9)	(3,9,0)	(0,3,4,5)	6(a,b,e) 6(c,d,g), 7(b)
7	T	T	TM	(3,9)	(3,9,0)	(0,3,6,3)	6(a-i)
8	M^{K1}	KR(1)-M	-	(3,9)	(3,8,1)	(1,2,3,6)	7(a)
9	M_K^{K1}	KR(1)-EMK	-	(3,8)	(3,7,1)	(1,2,2,6)	7(a)
10	T_H^V	VR-ETH	-	(3,8)	(3,7,1)	(1,2,3,5)	6(g)
11	A or T_H^H	A or HR-ETH	-	(3,7)	(3,7,0)	(1,2,2,5)	6(c), 7(b)
12	T_H	ETH	-	(3,7)	(3,7,0)	(1,2,4,3)	6(c,d,g), 7(b)
13	T_M^L or M^L	LR-ETM or LR-M	-	(3,9)	(3,7,2)	(2,1,4,5)	6(e) 6(b)
14	M^{K2}	KR(2)-M	-	(3,7)	(3,7,0)	(2,1,1,6)	7(a)
15	M or T_M^M	M or MR-ETM	SM	(3,7)	(3,7,0)	(2,1,2,5)	6(a,b,e), 7(a)
16	T_M	ETM	-	(3,7)	(3,7,0)	(2,1,4,3)	6(a,b,e)
17	M_K^{K2}	KR(2)-EMK	-	(3,6)	(3,6,0)	(2,1,0,6)	7(a)
18	M_K	EMK	-	(3,6)	(3,6,0)	(2,1,1,5)	7(a)
19	D^L	LR-D	-	(2,10)	(2,6,4)	(0,2,5,5)	7(b)
20	$D^{A,A}$	AAR-D	-	(2,8)	(2,6,2)	(0,2,2,6)	6(g), 7(b)
21	D^A	AR-D	-	(2,8)	(2,6,2)	(0,2,3,5)	7(b)
22	D or V^V or K^{K1}	D or VR-V or KR(1)-K	-	(2,8)	(2,6,2)	(0,2,4,4)	6(h), 7(a,b)
23	V^H	HR-V	-	(2,7)	(2,6,1)	(0,2,3,4)	6(d)
24	V	V	VSD	(2,7)	(2,6,1)	(0,2,5,2)	6(d,g,h)
25	H^L	LR-H	-	(2,9)	(2,5,4)	(1,1,4,5)	6(d)
26	H D_A^A	H or AR-EDA	HSD	(2,7)	(2,5,2)	(1,1,2,5)	6(c,d,h)
27	D_A	EDA	-	(2,7)	(2,5,2)	(1,1,3,4)	7(b)
28	K^{K2}	KR(2)-K	-	(2,6)	(2,5,1)	(1,1,2,4)	7(b)
29	K	K	-	(2,6)	(2,5,1)	(1,1,3,3)	7(b)
30	L(T)	L(T)	-	(1,9)	(1,3,6)	(0,1,6,3)	6(b)
31	$L(T_M)$	L(ETM)	-	(1,7)	(1,3,4)	(0,1,4,3)	6(b)
32	$L(T_H)$	L(ETH)	-	(1,7)	(1,3,4)	(0,1,5,2)	6(b)
33	L(M)	L(M)	-	(1,7)	(1,3,4)	(0,1,6,1)	6(b)

can be found. The central columns containing numbers correspond to three different classification schemes characterizing each site according to its neighborhood. The (n_1, n_2) column displays the number of first and second neighbors, the (n_1, n_2^d, n_2^i) column offers a split count of the second neighbors into direct and indirect second neighbors [13], and the $(n_1^s, n_1^b, n_2^s, n_2^b)$ column shows a split count of both the first and second neighborhoods into surface and bulk neighbors. The latter classification is due to Zhou *et al.* [19], and as can be seen, it is very useful in order to unambiguously distinguish between all the sites contained in the table.

III. ANALYTICAL SOLUTION OF THE ETCH RATES IN A CCA

As the central goal of this paper, we consider in this section the derivation of the analytical expressions for the etch rates of the different surface orientations in terms of a limited number of atomistic removal rates. The previous section has provided the necessary notation to effectively describe the realization of step flow on a wide variety of surfaces. This includes the definition of the restricted and edge terrace (and step) sites. In this section, we proceed first by presenting the fundamental ideas of the simulation method, providing then the full details of the theoretical derivation.

In the CCA method for the simulation of anisotropic etching, the substrate is treated as a collection of crystallographic sites (or, in general, cells) which can be fully or partially occupied (e.g., by atoms or any other "occupants"). The atoms have associated removal rates which depend on the site type (or cell type) they occupy, and the propagation of the surface is described as the overall result of gradually decreasing the occupation of the surface sites (or cells) according to the removal rates of the atoms (or occupants).

When we use the term "occupation" of a site, it corresponds to the "mass" of the occupying atom in the original presentation of the CCA method by Zhu and Liu [15]. We prefer to avoid the "mass" terminology for the following reasons: 1) The equations that we derive for the time dependence of the occupation of a site are based on a nondimensional character, which the
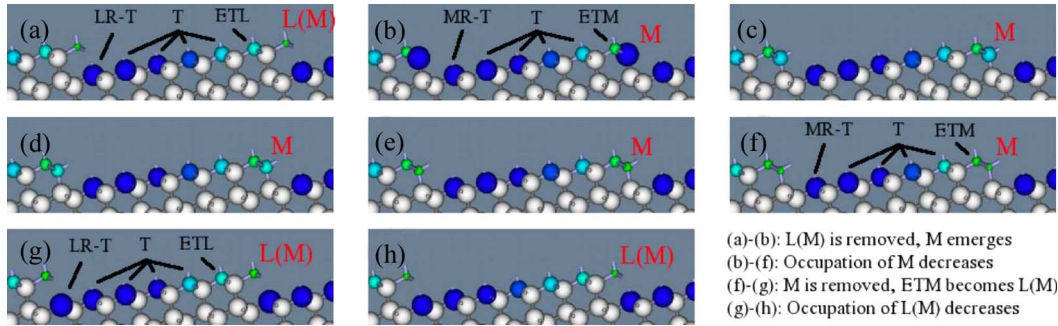
Fig. 8. Example of time evolution using the CCA method for (775). Time increases from (a) to (h).

occupation satisfies but the "mass" does not; 2) the crucial idea or starting principle of the CCA method is to recognize that the rate of decrease of the occupation of a site is equal to the rate of removal of the corresponding atom, without any need to involve the "mass" of the atoms; and 3) by decoupling the occupation of the sites from inherent properties of the occupants such as the "mass," the underlying geometrical nature of the CCA method can be perceived better.

If a site is on the surface, its occupation π has a value in the range [0, 1]. When the occupying atom first emerges to the surface due to the removal of neighboring atoms, π is 1. When the site is completely empty, π becomes 0. At every time step, the value of π is reduced by an amount $r\Delta t$ from its previous value, where Δt is the time increment (not necessarily constant) and r is the (possibly time-dependent) removal rate of the atom. This reduction in the occupation results simply from the fact that the rate of change in the occupation of the site ($-(\Delta\pi/\Delta t)$) is equal to the rate of the removal of the atom populating it (r), i.e., $-(\Delta\pi/\Delta t) = r$. In differential form, this is written as

$$\frac{d\pi}{dt} = -r. \qquad (1)$$

As an example, Fig. 8 shows the changes observed in the occupation of different surface sites during a sequence of constant time steps in the CCA evolution of the (775) orientation. In Fig. 8, the occupation of a surface site is described by the size and color of the occupying atoms, with the larger darker spheres corresponding to a larger occupation and the smaller lighter spheres being closer to the empty state. The bulk sites, whose occupation is 1, are represented by gray spheres with an arbitrary intermediate size. This allows highlighting the atoms which belong to the interface, separating them from the bulk. For this particular case, the rates of the removal of L(M), M, ETM, and T atoms satisfy the condition $r_{L(M)} > r_M > r_{ETM} \gg r_T$, chosen to mimic the step flow on this surface. In Fig. 8(a), site L(M) has a small occupation (small light-colored sphere), and the occupying atom has a large rate $r_{L(M)}$; therefore, this atom will be removed next. As shown in Fig. 8(b), this leads to the emergence of site M. As a new member of the surface, site M exhibits a value of 1 for the occupation [largest blue ball in Fig. 8(b)]. Since the removal rate for an M atom is larger than for ETM ($r_M > r_{ETM}$), the evolution in Fig. 8(b)–(f) essentially consists on the reduction

of the occupation of M. Note that the occupation of all the other sites (including ETM, T, MR-T,...) is also reduced, although this is not noticeable in the figure due to their small removal rates, resulting in small changes in occupation ($-r_{small}\Delta t = \Delta\pi_{small}$) and, thus, in the size and color of the corresponding spheres. In Fig. 8(g), M has been removed, and site ETM has become an L(M). In Fig. 8(h), the occupation of L(M) has been reduced, which is accompanied by small reductions in the occupation of the other sites, almost unnoticeable due to the small changes in the sizes of the spheres. At this point, the system is back on state (a), and the same processes will be repeated.

Note that the only physical input used for the evolution shown in Fig. 8 is that etching proceeds as a step-flow process, which is enforced by requiring that the removal rate of the terrace atoms is very low as compared to the rest of the atoms ($r_T \ll r_{others}$). As shown in the following section, except for this physical insight, the CCA is essentially a geometrical method in which the advancement of a crystallographic plane is replaced by the propagation of the occupation field defined all over the smaller constituting elements of the plane, i.e., the surface sites (or cells).

Taking into account that the removal rate of a surface atom will typically change with time (e.g., due to a change in the neighborhood, such as the ETM becoming an L(M) in the previous example), we can formally describe the value of the occupation at any instant t by integrating (1) to arrive at the following integral form:

$$\pi(t) = 1 - \int_0^t r(t')dt' \qquad (2)$$

where the initial condition $\pi(0) = 1$ has been used. When the atom is removed at time $t = \tau$, we have $\pi(\tau) = 0$, and (2) becomes

$$\int_0^\tau r(t')dt' = 1. \qquad (3)$$

Equation (3) provides a way to calculate the elapsed time τ between the birth and the removal of a surface atom if we know the history of the atom, i.e., if we know how many times the site type of the atom changes, what are the removal rates for

those site types, and what is the time interval spent as each type. As an example, the L(M) atoms in Fig. 8 emerge to the surface as LR-T type and successively become MR-T, T, and ETM atoms before they are converted into the L(M) type, which is when they are removed. Equation (3) will become our working principle in order to derive the analytical expressions that describe the overall etch rate of any surface orientation as a function of the atom removal rates and a few geometrical features.

A. Derivation of the Etch Rates

We are interested in the determination of the overall etch rate of any surface orientation when the propagation of the surface is realized by using the CCA method, e.g., as shown in Fig. 8. In most cases, the structure of the surface repeats itself after some time period. For instance, in Fig. 8, the period spans two events, namely, the removal of the M and L(M) atoms. Due to this feature, the etch rate can be calculated as the ratio of the advanced distance in one such period to the corresponding time

$$R = \frac{\Delta H}{\Delta t} = \frac{\Delta H_P + \Delta H_Q}{\Delta t_P + \Delta t_Q}. \tag{4}$$

Here, ΔH_P and ΔH_Q are the changes in the average height of the surface when the atoms of generic types P and Q are removed, respectively, and Δt_P and Δt_Q are the corresponding time increments. In Fig. 8, the generic sites P and Q are M and L(M), respectively.

1) Determination of the Change in the Average Height: In order to determine ΔH_P and ΔH_Q, we use the spatial periodicity of the surface in the horizontal direction and restrict the analysis to one such repeated structure, as shown in Fig. 9. Before the removal of a row of M atoms, the average height of the surface is $\langle H \rangle^{(i)} = (\Sigma_{i=1}^N H_i)/N = (H_1 + H_2 + \cdots + H_7)/7$, where $N = 7$ is the number of surface atoms in the repeated region. After the removal of the M-type atoms, the average height is $\langle H \rangle^{(f)} = (\Sigma_{i=2}^{N+1} H_i)/N = (H_2 + H_3 + \cdots + H_8)/7$. Thus, the change in the average position of the surface is

$$\begin{aligned}
\Delta H_M &= \langle H \rangle^{(f)} - \langle H \rangle^{(i)} \\
&= \frac{H_8 - H_1}{7} \\
&= \frac{H_{LR-T} - H_M}{7} \\
&= -\frac{d \cos \alpha}{N}.
\end{aligned} \tag{5}$$

Note that $d \cos \alpha = H_M - H_{LR\text{-}T}$ is the projection (along the z-direction) of the distance between the removed (M) and the emerging (LR-T) atoms. This result can be generalized, and the change in the average height can be obtained simply as the projection (along the z-direction) of the distance between the removed (R) and the emerging (E) atoms divided by the number of atoms in the repeated structure

$$\Delta H_R = \frac{H_E - H_R}{N} = -\frac{d_{R-E} \cos \alpha}{N}. \tag{6}$$
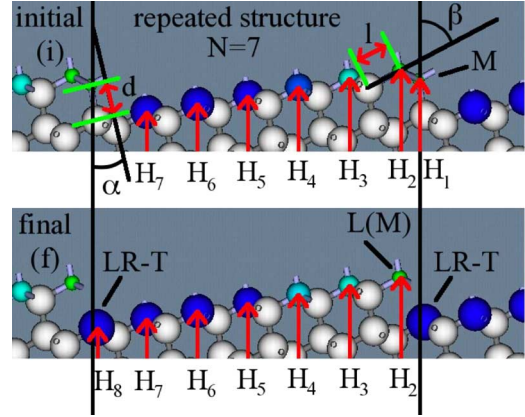

Fig. 9. Geometry for the determination of ΔH_M and $\Delta H_{L(M)}$ on (775).

For instance, the removal of the L(M) atoms on (775) in Fig. 9 leads to the expression

$$\Delta H_{L(M)} = \frac{H_M - H_{L(M)}}{7} = -\frac{l \cos \beta}{N} \tag{7}$$

which corresponds to substituting in (6) the emerging atom E by M and the removed atom R by L(M). Similar expressions are found for other surface orientations involving the removal and the emergence of other atom types, and (6) is always found to be valid.

Note that, in Fig. 9, $d = l = (\sqrt{3}a/4)$, where a is the lattice parameter of the conventional unit cell of the diamond structure of crystalline silicon ($a = 5.43$ Å). Since α can be understood as the angle between the planes (775) and (111), we have $\cos \alpha = [(1,1,1) \cdot (7,7,5)]/(\sqrt{1^2 + 1^2 + 1^2}\sqrt{7^2 + 7^2 + 5^2}) = 19/(\sqrt{3}\sqrt{123})$. Similarly, β is the angle between (775) and $(11\bar{1})$. Thus, one gets $\cos \beta = [(1,1,-1) \cdot (7,7,5)]/(\sqrt{1^2 + 1^2 + (-1)^2}\sqrt{7^2 + 7^2 + 5^2}) = 9/(\sqrt{3}\sqrt{123})$. As a result, the total displacement in the average position of the surface is

$$\begin{aligned}
\Delta H &= \Delta H_M + \Delta H_{L(M)} \\
&= -\frac{\sqrt{3}a(\cos \alpha + \cos \beta)}{4 \cdot 7} \\
&= -\frac{a}{\sqrt{123}}.
\end{aligned} \tag{8}$$

Following the same recipe, the previous result can be easily generalized for the whole M_T subfamily $(h + 2 \ h + 2 \ h)$ to which (775) belongs ($h = 5$). One finds

$$\Delta H_M = -\frac{(3h + 4)a}{4(h + 2)\sqrt{3h^2 + 8h + 8}} \tag{9}$$

$$\Delta H_{L(M)} = -\frac{(h + 4)a}{4(h + 2)\sqrt{3h^2 + 8h + 8}} \tag{10}$$

$$\begin{aligned}
\Delta H &= \Delta H_M + \Delta H_{L(M)} \\
&= -\frac{a}{\sqrt{3h^2 + 8h + 8}}.
\end{aligned} \tag{11}$$

Note that the horizontal periodicity (i.e., the number of atoms in the horizontally repeated structure) in this family is $h + 2$ since there are h terrace sites and two step sites (M and

TABLE IV
$\Delta H = \Delta H_{\mathrm{P}} + \Delta H_{\mathrm{Q}}$ for the Major Surface Families Under Step Flow. Step Propagation Involves the Removal of Rows of Type P and Q Atoms in Alternation ($a = 5.43$ Å Is the Lattice Parameter of the Conventional Unit Cell)

Family	h	Condition	Case	P	Q	$-\Delta H_{\mathrm{P}}$	$-\Delta H_{\mathrm{Q}}$	$-\Delta H$
(100)				D	-	$\frac{a}{4}$	-	$\frac{a}{4}$
(110)				M	-	$\frac{\sqrt{2}a}{4}$	-	$\frac{a}{2\sqrt{2}}$
(111)				T	L(T)	$\frac{a}{4\sqrt{3}}$	$\frac{\sqrt{3}a}{4}$	$\frac{a}{\sqrt{3}}$
K_{T} (h+2 h 0)	any	$r_{\mathrm{K}} > r_{\mathrm{EMK}}$	$h \geq 2$	K	-	$\frac{a}{2\sqrt{2h^2+4h+4}}$	-	$\frac{a}{2\sqrt{2h^2+4h+4}}$
K_{S} (h 1 0)	odd	$r_{\mathrm{KR(2)-K}} >$	$h \geq 3$	KR(2)-K	-	$\frac{a}{2\sqrt{h^2+1}}$	-	$\frac{a}{2\sqrt{h^2+1}}$
	even	$r_{\mathrm{KR(1)-EMK}}$				$\frac{a}{4\sqrt{h^2+1}}$	-	$\frac{a}{4\sqrt{h^2+1}}$
M_{T} (h+2 h+2 h)	any	$r_{\mathrm{M}} > r_{\mathrm{ETM}}$	$h \geq 2$	M	L(M)	$\frac{(3h+4)a}{4(h+2)\sqrt{3h^2+8h+8}}$	$\frac{(h+4)a}{4(h+2)\sqrt{3h^2+8h+8}}$	$\frac{a}{\sqrt{3h^2+8h+8}}$
		$r_{\mathrm{M}} < r_{\mathrm{ETM}}$		L(ETM)	ETM			
M_{S} (h h 1)	odd	$r_{\mathrm{M}} > r_{\mathrm{ETM}}$	$h \geq 3$	M	L(M)	$\frac{2(h+1)a}{4h\sqrt{2h^2+1}}$	$\frac{2(h-1)a}{4h\sqrt{2h^2+1}}$	$\frac{a}{\sqrt{2h^2+1}}$
		$r_{\mathrm{M}} < r_{\mathrm{ETM}}$		L(ETM)	ETM			
	even	$r_{\mathrm{M}} > r_{\mathrm{ETM}}$		M	L(M)	$\frac{2(h+1)a}{8h\sqrt{2h^2+1}}$	$\frac{2(h-1)a}{8h\sqrt{2h^2+1}}$	$\frac{a}{2\sqrt{2h^2+1}}$
		$r_{\mathrm{M}} < r_{\mathrm{ETM}}$		L(ETM)	ETM			
D_{T} (h+2 h h)	any	$(r_{\mathrm{H}} > r_{\mathrm{A}} \rightarrow)$	$h = 2$	H	V	$\frac{(3h+2)a}{4(h+1)\sqrt{3h^2+4h+4}}$	$\frac{(h+2)a}{4(h+1)\sqrt{3h^2+4h+4}}$	$\frac{a}{\sqrt{3h^2+4h+4}}$
		$r_{\mathrm{H}} > r_{\mathrm{ETH}}$	$h \geq 3$	H	V			
		$(r_{\mathrm{H}} < r_{\mathrm{A}} \rightarrow)$	$h = 2$	L(ETH)	A	$\frac{(3h+2)a}{4(h+1)\sqrt{3h^2+4h+4}}$	$\frac{(h+2)a}{4(h+1)\sqrt{3h^2+4h+4}}$	$\frac{a}{\sqrt{3h^2+4h+4}}$
		$r_{\mathrm{H}} < r_{\mathrm{ETH}}$	$h \geq 3$	L(ETH)	ETH			
D_{S} (h 1 1)	odd	$(r_{\mathrm{H}} > r_{\mathrm{A}} \rightarrow)$	$h = 3$	H	V	$\frac{(h+2)a}{2(h+1)\sqrt{h^2+2}}$	$\frac{ha}{2(h+1)\sqrt{h^2+2}}$	$\frac{a}{\sqrt{h^2+2}}$
		$r_{\mathrm{EDA}} > r_{\mathrm{A}}$	$h \geq 5$	EDA	HR-V			
		$(r_{\mathrm{H}} < r_{\mathrm{A}} \rightarrow)$	$h = 3$	L(ETH)	A			
		$r_{\mathrm{EDA}} < r_{\mathrm{A}}$	$h \geq 5$	L(ETH)	A			
	even	$(r_{\mathrm{H}} > r_{\mathrm{A}} \rightarrow)$	$h = 4$	H	V	$\frac{(h+2)a}{4(h+1)\sqrt{h^2+2}}$	$\frac{ha}{4(h+1)\sqrt{h^2+2}}$	$\frac{a}{2\sqrt{h^2+2}}$
		$r_{\mathrm{EDA}} > r_{\mathrm{A}}$	$h \geq 6$	EDA	HR-V			
		$(r_{\mathrm{H}} < r_{\mathrm{A}} \rightarrow)$	$h = 4$	L(ETH)	A			
		$r_{\mathrm{EDA}} < r_{\mathrm{A}}$	$h \geq 6$	L(ETH)	A			

ETM) (see Fig. 1). Interestingly, the expression for ΔH for the whole family does not change when the relative removal rates of the M and ETM atoms are inverted, thus providing a different realization of step flow on these surfaces. In Figs. 8 and 9, etching proceeds as a step-flow process where the M and the L(M) atoms are removed sequentially. This is due to the choice that $r_{\mathrm{M}} > r_{\mathrm{ETM}}$. In the reverse case, $r_{\mathrm{ETM}} > r_{\mathrm{M}}$, etching still occurs as a step-flow process, but now, it proceeds by sequentially removing the ETM and L(ETM) atoms. In this case, one gets

$$\Delta H_{\mathrm{ETM}} = -\frac{(h+4)a}{4(h+2)\sqrt{3h^2+8h+8}} \tag{12}$$

$$\Delta H_{\mathrm{L(ETM)}} = -\frac{(3h+4)a}{4(h+2)\sqrt{3h^2+8h+8}} \tag{13}$$

$$\Delta H = \Delta H_{\mathrm{ETM}} + \Delta H_{\mathrm{L(ETM)}}$$
$$= -\frac{a}{\sqrt{3h^2+8h+8}} \tag{14}$$

which demonstrates that the total advancement of the surface is identical in both realizations of the step-flow process.

A similar geometrical analysis can be carried out for the other surface families (M_{S}, D_{T}, D_{S}, K_{T}, and K_{S}). The results of such study have been gathered in Table IV. In some cases, ΔH takes different values depending on whether the Miller index h is even ($h = 2n$) or odd ($h = 2n + 1$). However, it does not typically depend on the particular realization of step flow obtained by changing the relative values of the removal rates for sites located right at the steps and at the edges of the steps. One should realize, however, that certain choices of the removal rates can produce a rather complicated nonstep-flow time evolution (Section III-A2).

2) Determination of the Time Increment: In order to determine the time increments Δt_{P} and Δt_{Q} corresponding to the atom removals at the P and Q generic sites [see (4)], we pay attention to the site-type history of each atom and use (3) to generate two implicit equations containing the two time increments. By solving the resulting system of equations, the time increments can be determined.
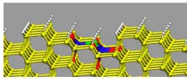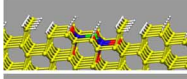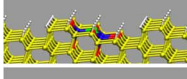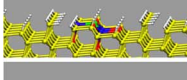
Current neighborhood	Current occupation	Exposed as site	Exposed for time	Occupation will be reduced by
	$\pi_1 = 1$	HR-T	Δt_{ETH}	$r_{\text{HR}-\text{T}}\Delta t_{\text{ETH}}$
	$\pi_2 = \pi_1 - r_{\text{HR}-\text{T}}\Delta t_{\text{ETH}}$	HR-T	$\Delta t_{\text{L(ETH)}}$	$r_{\text{HR}-\text{T}}\Delta t_{\text{L(ETH)}}$
	$\pi_3 = \pi_2 - r_{\text{HR}-\text{T}}\Delta t_{\text{L(ETH)}}$	T	Δt_{ETH}	$r_{\text{T}}\Delta t_{\text{ETH}}$
	$\pi_4 = \pi_3 - r_{\text{T}}\Delta t_{\text{ETH}}$	ETH	$\Delta t_{\text{L(ETH)}}$	$r_{\text{ETH}}\Delta t_{\text{L(ETH)}}$
	$\pi_5 = \pi_4 - r_{\text{ETH}}\Delta t_{\text{L(ETH)}}$	ETH	Δt_{ETH}	$r_{\text{ETH}}\Delta t_{\text{ETH}}$
	$\pi_6 = \pi_5 - r_{\text{ETH}}\Delta t_{\text{ETH}} = 0$	removed	-	-
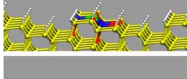
Fig. 10. History of the ETH atoms according to the CCA evolution of (533) with $r_{\text{L(ETH)}} > r_{\text{ETH}} > r_{\text{H}} \gg r_{\text{T}}$.
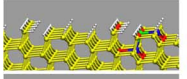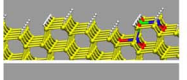
Current neighborhood	Current occupation	Exposed as site	Exposed for time	Occupation will be reduced by
	$\pi_1 = 1$	LR-H	$\Delta t_{\text{L(ETH)}}$	$r_{\text{LR}-\text{H}}\Delta t_{\text{L(ETH)}}$
	$\pi_2 = \pi_1 - r_{\text{LR}-\text{H}}\Delta t_{\text{L(ETH)}}$	H	Δt_{ETH}	$r_{\text{H}}\Delta t_{\text{ETH}}$
	$\pi_3 = \pi_2 - r_{\text{H}}\Delta t_{\text{ETH}}$	L(ETH)	$\Delta t_{\text{L(ETH)}}$	$r_{\text{L(ETH)}}\Delta t_{\text{L(ETH)}}$
	$\pi_4 = \pi_3 - r_{\text{L(ETH)}}\Delta t_{\text{L(ETH)}} = 0$	removed	-	-
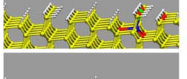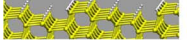
Fig. 11. History of the L(ETH)atoms according to the CCA evolution of (533) with $r_{\text{L(ETH)}} > r_{\text{ETH}} > r_{\text{H}} \gg r_{\text{T}}$.

As an example, Figs. 10 and 11 show the site-type history of the ETH and L(ETH) atoms for a step-flow realization of etching on the (533) orientation when $r_{\text{L(ETH)}} > r_{\text{ETH}} > r_{\text{H}} \gg r_{\text{T}}$. According to the first row in Fig. 10, the ETH atoms appear on the surface as type HR-T, and observe the removal of ETH atoms, which lasts for a time Δt_{ETH}. Thus, their occupation is reduced by the amount $r_{\text{HR-T}}\Delta t_{\text{ETH}}$, as shown in row 2. At this stage, the atoms are still considered as type HR-T since their neighborhoods, which reach to the second neighbors (but not further), have not changed. In this state, the atoms will be exposed to the etchant for a time $\Delta t_{\text{L(ETH)}}$, which is necessary to remove the L(ETH) atoms. As a result, their occupation is reduced by $r_{\text{HR-T}}\Delta t_{\text{L(ETH)}}$ from the previous value, as shown in row 3. At this stage, the atoms have become of type T and remain as such for a time Δt_{ETH}, which is the interval required for the ETH atoms to be removed. In row 4, the current occupation of the atoms has been reduced accordingly. Now, the atoms have become type ETH and will be exposed to the etchant during the removal of the L(ETH) atoms, resulting in a reduction of their occupation by the amount $r_{\text{ETH}}\Delta t_{\text{L(ETH)}}$. After this, in row 5, the atom type has not changed since the state of the neighborhood has not

changed either. Now, it is the time for the atoms themselves to leave, reducing their occupation by $r_{\text{ETH}}\Delta t_{\text{ETH}}$ and reaching the zero value, as shown in row 6. We can expand the equation in row 6 to get

$$r_{\text{HR-T}}\Delta t_{\text{ETH}} + r_{\text{HR-T}}\Delta t_{\text{L(ETH)}} + r_{\text{T}}\Delta t_{\text{ETH}}$$
$$+ r_{\text{ETH}}\Delta t_{\text{L(ETH)}} + r_{\text{ETH}}\Delta t_{\text{ETH}} = 1. \quad (15)$$

Equation (15) can be directly compared to (3). It states that the total reduction in the occupation of the atoms is 1. Note that (15) can be simply written by summing all the elements of the fifth column in Fig. 10 and equating them to 1. This simple rule makes it very easy to apply (3) to each particular example. For instance, by considering the fifth column in Fig. 11, we can write down the equation for the history of the L(ETH) atoms as follows:

$$r_{\text{LR-H}}\Delta t_{\text{L(ETH)}} + r_{\text{H}}\Delta t_{\text{ETH}} + r_{\text{L(ETH)}}\Delta t_{\text{L(ETH)}} = 1. \quad (16)$$

Equations (15) and (16) form a system of two equations with two unknowns, namely, Δt_{ETH} and $\Delta t_{\text{L(ETH)}}$. The system can

be rewritten in matrix form as

$$
\begin{pmatrix} \overbrace{r_{\text{HR-T}} + r_{\text{T}} + r_{\text{ETH}}}^{A} & \overbrace{r_{\text{HR-T}} + r_{\text{ETH}}}^{B} \\ \underbrace{r_{\text{H}}}_{C} & \underbrace{r_{\text{LR-H}} + r_{\text{L(ETH)}}}_{D} \end{pmatrix}
$$
$$
\cdot \begin{pmatrix} \Delta t_{\text{ETH}} \\ \Delta t_{\text{L(ETH)}} \end{pmatrix} = \begin{pmatrix} 1 \\ 1 \end{pmatrix}. \quad (17)
$$

Solving the system, we get

$$
\Delta t_{\text{ETH}} = \frac{D - B}{AD - BC} \tag{18}
$$
$$
\Delta t_{\text{L(ETH)}} = \frac{A - C}{AD - BC}. \tag{19}
$$

Therefore, the total time increment $\Delta t = \Delta t_{\text{P}} + \Delta t_{\text{Q}} = \Delta t_{\text{ETH}} + \Delta t_{\text{L(ETH)}}$ is calculated as

$$
\Delta t = \frac{(A + D) - (B + C)}{AD - BC}. \tag{20}
$$

The etch rate $R = \Delta H / \Delta t$ for (533) can then be written as in (21), shown at the bottom of the page, by using the value of ΔH from Table V (corresponding to the row for D_{T} and $h = 3$) and the value for Δt obtained from (17) and (20).

The previous derivation of the etch rate for (533) assumes that $r_{\text{ETH}} > r_{\text{H}}$. In the reverse situation, $r_{\text{H}} > r_{\text{ETH}}$, step flow will proceed by a sequential removal of H and V atom rows. Taking into account the site-type history for these two atoms, as shown in Fig. 12, it is straightforward to derive the system of two equations for the corresponding time increments Δt_{H} and Δt_{V} using the general principle of (3). In matrix form, the system of equations is written using the values for A, B, C, and D given in Table V (corresponding to the row for D_{T}, $r_{\text{H}} > r_{\text{ETH}}$, and $h = 3$). Thus, the etch rate of (533) becomes

$$
R_{(533)} = -\frac{a}{\sqrt{43}} \frac{r_{\text{H}}(r_{\text{VR-T}} + r_{\text{T}} + r_{\text{ETV}} + r_{\text{V}})}{(r_{\text{H}} + r_{\text{VR-T}} + r_{\text{ETV}} + r_{\text{V}} - r_{\text{HR-T}} - r_{\text{ETH}})},
$$
$$
r_{\text{H}} > r_{\text{ETH}}. \tag{22}
$$

Although ΔH remains the same for both realizations of step flow, the final expression for the etch rate is very different depending on the relative rates of the H and ETH atoms.

Similar studies can be performed for other surface orientations in order to derive the etch rate of the plane as a function of the removal rates of the atoms appearing on the surface. In most cases, it is even possible to write down a global expression for the etch rate of each main surface family M_{T}, M_{S}, D_{T}, etc... depending only on the Miller index h and the removal rates. The results of the study are summarized in Table V, which displays the values of matrix coefficients A, B, C, and D. In some cases, such as the M_{S} family with odd values for h and $r_{\text{M}} > r_{\text{ETM}}$, the global expression cannot be obtained. In

these cases, we offer one or two examples of values for specific orientations. Also, there are situations such as that for (441) when $r_{\text{M}} > r_{\text{ETM}}$, which lead to a very complex evolution of the surface, involving more than two time increments and, thus, larger matrices and more coefficients than A through D. As it turns out, these cases are not essential for the overall performance of a CCA simulation and can normally be avoided.

For completeness and reference, Table VI shows the etch rate of the three main orientations and the first two surfaces of each subfamily under the specified particular set of conditions. In spite of the simplicity of the step-flow process enforced on each surface, the final expressions for the etch rates are rather complex. Under more complex choices for the removal rates, the equations become even more complicated, and in some cases, they cannot be determined explicitly.

IV. FIT TO EXPERIMENTS

Once the equations linking the etch rate of each orientation to the atomistic removal rates have been determined, it is natural to wonder whether it is possible to solve these equations for the removal rates using the experimental etch rates as an input. For instance, it is straightforward to solve r_{D} and r_{M} if the etch rates of (100) and (110) are known. Is it also possible to solve the rest of the equations in Table VI?

Unfortunately, in that form, the equations cannot be solved as they are strongly coupled, and more importantly, they contain a large number of unknowns, easily surpassing the number of equations. In fact, the large number of variables in comparison to the number of equations becomes a serious limitation when one considers the typical number of experimental etch rates available (which corresponds to the number of equations in the system), normally including only the three main orientations and a few other planes.

A. Procedure

For the purpose of fitting the atomistic removal rates, we consider a simplified version of the equations based on a reduction in the number of different removal rates, as shown in Table VII. In these equations, the effect of restriction on the etch rates has been dropped (i.e., disregarded), and only the effect of edging is maintained. As an example, the restricted site MR-T is considered to have the same rate as the unrestricted T, i.e., $r_{\text{MR-T}} = r_{\text{T}}$. The same happens to LR-M, which is considered as M, and the scheme is similarly applied to other restricted sites. Also, according to the notion of a neighborhood containing up to the second neighbors, site ETV is actually identical to T. Thus, $r_{\text{VR-ETV}} = r_{\text{ETV}}$ because of disregarding the effect of restriction, and $r_{\text{ETV}} = r_{\text{T}}$ because the neighborhoods are identical. As a result, $r_{\text{VR-ETV}} = r_{\text{T}}$.

On the contrary, the effect of edging on the etch rates is considered to be a key feature of the overall analysis and

$$
R_{(533)} = -\frac{a}{\sqrt{43}} \frac{(r_{\text{HR-T}} + r_{\text{T}} + r_{\text{ETH}})(r_{\text{LR-H}} + r_{\text{L(ETH)}}) - (r_{\text{HR-T}} + r_{\text{ETH}})r_{\text{H}}}{r_{\text{T}} + r_{\text{LR-H}} + r_{\text{L(ETH)}} - r_{\text{H}}}, \qquad r_{\text{ETH}} > r_{\text{H}} \tag{21}
$$

TABLE V

ETCH RATE $R = \Delta H/\Delta t$ FOR THE MAJOR SURFACE FAMILIES UNDER STEP PROPAGATION. $\Delta t = [(A+D) - (B+C)]/AD - BC]$, EXCEPT IF $A \neq 0$ AND $B = C = D = 0$, WHERE $R = \Delta H \cdot A$ ($a = 5.43$ Å IS THE LATTICE PARAMETER)

Family	h	$-\Delta H$	Condition	Case	A	B	C	D
(100)		$\frac{a}{4}$			r_D	0	0	0
(110)		$\frac{a}{2\sqrt{2}}$			r_M	0	0	0
(111)		$\frac{a}{\sqrt{3}}$			$\frac{r_T r_{L(T)}}{r_T+r_{L(T)}}$	0	0	0
K_T (h+2 h 0), h≥2	any	$\frac{a}{2\sqrt{2h^2+4h+4}}$	$r_K > r_{EMK}$	h = 2	$r_{KR(1)-M}+r_{KR(2)-EMK}+r_K$	0	0	0
				h ≥ 3	$r_{KR(1)-M}+r_{KR(2)-M}+(h-3)r_M+r_{EMK}+r_K$	0	0	0
K_S (h 1 0), h≥3	odd	$\frac{a}{2\sqrt{h^2+1}}$	$r_{KR(2)-K} > r_{KR(1)-EMK}$	h ≥ 3	$r_{KR(1)-EMK}+\frac{h-3}{2}r_D+\ r_{KR(2)-K}$	0	0	0
	even	$\frac{a}{4\sqrt{h^2+1}}$		h ≥ 4	$2r_{KR(1)-EMK}+\frac{h-2}{2}r_D+\ 2r_{KR(2)-K}$	0	0	0
M_T (h+2 h+2 h), h≥2	any	$\frac{a}{\sqrt{3h^2+8h+8}}$	$r_M > r_{ETM}$	h ≥ 2	r_M	0	$r_{MR-T}+(h-1)r_T+r_{ETM}$	$r_{LR-T}+h r_T+r_T+r_{L(M)}$
			$r_M < r_{ETM}$		$r_{MR-T}+(h-1)r_T+r_{ETM}$	$r_{MR-T}+(h-2)r_T+r_{ETM}$	r_M	$r_{LR-M}+r_{L(ETM)}$
M_S (h h 1), h≥3	odd	$\frac{a}{\sqrt{2h^2+1}}$	$r_M > r_{ETM}$	h = 3	r_M	0	$r_{MR-T}+r_{ETM}$	$r_{LR-T}+r_{ETL}+r_{L(M)}$
			$r_M < r_{ETM}$	h ≥ 5	requires larger matrix	-	-	-
	even	$\frac{a}{2\sqrt{2h^2+1}}$	$r_M > r_{ETM}$	h ≥ 3	$r_{MR-T}+\frac{h-3}{2}r_M+r_{ETM}$	$\frac{h-1}{2}r_M$	$\frac{h-1}{2}r_M$	$r_{LR-M}+\frac{h-3}{2}r_M+r_{L(ETM)}$
			$r_M < r_{ETM}$	h ≥ 4	requires larger matrix	-	-	-
				h ≥ 4	$2r_{MR-T}+(h-3)r_M+2r_{ETM}$	$r_{MR-T}+(h-3)r_M+2r_{ETM}$	$(h-1)r_M$	$r_{LR-M}+(h-2)r_M+r_{L(ETM)}$
D_T (h+2 h h), h≥2	any	$\frac{a}{2\sqrt{3h^2+4h+4}}$	$(r_H > r_A \rightarrow)$	h = 2	r_H	0	$r_{HR-T}+(h-2)r_T+r_{ETH}$	$r_{VR-T}+(h-2)r_T+r_{ETV}+r_V$
			$r_H > r_{ETH}$	h ≥ 3	r_H	0	$r_{HR-T}+(h-2)r_T+r_{ETH}$	$r_{VR-T}+(h-2)r_T+r_{ETV}+r_V$
			$(r_H < r_A \rightarrow)$	h = 2	$r_{HR-T}+r_{ETH}$	r_A	r_H	$r_{LR-H}+r_{L(ETH)}$
			$r_H < r_{ETH}$	h ≥ 3	$r_{HR-T}+(h-2)r_T+r_{ETH}$	$r_{HR-T}+(h-3)r_T+r_{ETH}$	r_H	$r_{LR-H}+r_{L(ETH)}$
	odd	$\frac{a}{\sqrt{h^2+2}}$	$(r_H < r_A \rightarrow)$	h = 3	r_H	0	r_A	$r_{VR-ETV}+r_V$
D_S (h 1 1), h≥3	odd	$\frac{a}{\sqrt{h^2+2}}$	$r_{EDA} > r_A$	h ≥ 5	$r_{AR-D}+r_{EDA}$	$r_{LR-D}+r_{L(ETH)}$	r_A	0
			$r_{EDA} > r_A$	h ≥ 7	$r_{AR-D}+\frac{h-5}{2}r_D+r_{EDA}$	$r_{LR-D}+\frac{h-3}{2}r_D+r_{L(ETH)}$	r_A	0
			$(r_H > r_A \rightarrow)$	h = 3	r_H	r_H	$2r_H$	r_H
			$r_{EDA} < r_A$	h ≥ 5	$r_{AR-D}+\frac{h-5}{2}r_D+r_{EDA}$	$r_{AR-D}+\frac{h-7}{2}r_D+r_{EDA}$	r_A	$r_{AR-D}+\frac{h-7}{2}r_D+r_{EDA}$
	even	$\frac{a}{2\sqrt{h^2+2}}$	$(r_H > r_A \rightarrow)$	h = 4	$r_{VR-ETH}+r_A+r_{HR-V}$	$r_{VR-ETH}+r_A+r_{HR-V}$	r_A	$r_{VR-ETH}+r_{HR-V}$
			$r_{EDA} > r_A$	h = 6	$2(r_{VR-ETH}+r_{HR-V})$	$2(r_{VR-ETH}+r_{HR-V})$	$2r_H$	$r_{VR-ETH}+r_{HR-V}$
			$r_{EDA} > r_A$	h ≥ 8	$2(r_{VR-ETH}+r_{HR-V})$	$2(r_{VR-ETH}+r_{HR-V})$	r_A	$r_{VR-ETH}+r_{HR-V}$
			$(r_H < r_A \rightarrow)$	h = 4	elaborated expressions	-	-	-
			$r_{EDA} < r_A$	h ≥ 6	$2r_{AR-D}+\frac{h-4}{2}r_D+2r_{EDA}$	$2r_{AR-D}+\frac{h-2}{2}r_D+2r_{EDA}$	r_A	0

Current neighborhood	Current occupation	Exposed as site	Exposed for time	Occupation will be reduced by
	$\pi_1 = 1$	H	Δt_H	$r_H \Delta t_H$
	$\pi_2 = \pi_1 - r_H \Delta t_H = 0$	removed	-	-

Current neighborhood	Current occupation	Exposed as site	Exposed for time	Occupation will be reduced by
	$\pi_1 = 1$	VR-T	Δt_V	$r_{VR-T} \Delta t_V$
	$\pi_2 = \pi_1 - r_{VR-T} \Delta t_V$	HR-T	Δt_H	$r_{HR-T} \Delta t_H$
	$\pi_3 = \pi_2 - r_{HR-T} \Delta t_H$	T	Δt_V	$r_T \Delta t_V$
	$\pi_4 = \pi_3 - r_T \Delta t_V$	T	Δt_H	$r_T \Delta t_H$
	$\pi_5 = \pi_4 - r_T \Delta t_H$	ETV	Δt_V	$r_{ETV} \Delta t_V$
	$\pi_6 = \pi_5 - r_{ETV} \Delta t_V$	ETH	Δt_H	$r_{ETH} \Delta t_H$
	$\pi_7 = \pi_6 - r_{ETH} \Delta t_H$	V	Δt_V	$r_V \Delta t_V$
	$\pi_8 = \pi_7 - r_V \Delta t_V = 0$	removed	-	-

Fig. 12. History of the H and V atoms according to the CCA evolution of (533) with $r_V > r_H > r_{ETH} \gg r_T$.

TABLE VI
Some Examples of Etch Rates for Step Flow According to the CCA Method ($a = 5.43$ Å Is the Lattice Parameter

	$R_{100} = \frac{a}{4} r_D$		
	$R_{110} = \frac{a}{2\sqrt{2}} r_M$		
	$R_{111} = \frac{a}{\sqrt{3}} \frac{r_T r_{L(T)}}{r_T + r_{L(T)}}$		
K_T	$R_{210} = \frac{a}{4\sqrt{5}} (r_{KR(1)-M} + r_{KR(2)-EMK} + r_K)$	$r_K > r_{EMK}$	
	$R_{530} = \frac{a}{2\sqrt{34}} (r_{KR(1)-M} + r_{KR(2)-M} + r_{EMK} + r_K)$	”	
K_S	$R_{310} = \frac{a}{2\sqrt{10}} (r_{KR(1)-EMK} + r_{KR(2)-K})$	$r_{KR(2)-K} > r_{KR(1)-EMK}$	
	$R_{410} = \frac{a}{4\sqrt{17}} (2 r_{KR(1)-EMK} + r_D + 2 r_{KR(2)-K})$	”	
M_T	$R_{221} = \frac{a}{6} \frac{(r_{MR-T}+r_T+r_{ETM})(r_{LR-M}+r_{L(ETM)}) - r_M(r_{MR-T}+r_{ETM})}{r_T+r_{LR-M}+r_{L(ETM)}-r_M}$	$r_{ETM} > r_M$	
	$R_{553} = \frac{a}{\sqrt{59}} \frac{(r_{MR-T}+2r_T+r_{ETM})(r_{LR-M}+r_{L(ETM)}) - r_M(r_{MR-T}+r_T+r_{ETM})}{r_T+r_{LR-M}+r_{L(ETM)}-r_M}$	”	
M_S	$R_{331} = \frac{a}{\sqrt{19}} \frac{(r_{MR-T}+r_{ETM})(r_{LR-M}+r_{L(ETM)}) - r_M^2}{r_{MR-T}+r_{LR-M}+r_{ETM}+r_{L(ETM)}-2r_M}$	$r_{ETM} > r_M$	
	$R_{441} = \frac{a}{2\sqrt{33}} \frac{(2r_{MR-T}+r_M+2r_{ETM})(r_{LR-M}+2r_M+r_{L(ETM)}) - 3r_M(r_{MR-T}+2r_M+r_{ETM})}{r_{MR-T}+r_{ETM}+r_{LR-M}+r_{L(ETM)}-2r_M}$	”	
D_T	$R_{211} = \frac{a}{2\sqrt{6}} \frac{r_H(r_{VR-T}+r_{ETV}+r_V)}{r_H+r_{VR-T}+r_{ETV}+r_V-r_{HR-T}-r_{ETH}}$	$r_H > r_A$	
	$R_{533} = \frac{a}{\sqrt{43}} \frac{r_H(r_{VR-T}+r_T+r_{ETV}+r_V)}{r_H+r_{VR-T}+r_{ETV}+r_V-r_{HR-T}-r_{ETH}}$	$r_H > r_{ETH}$	
D_S	$R_{311} = \frac{a}{\sqrt{11}} \frac{r_H(r_{VR-ETV}+r_V)}{r_H+r_{VR-ETV}+r_V-r_A}$	$r_H > r_A$	
	$R_{411} = \frac{a}{2\sqrt{18}} \frac{r_H(r_{VR-ETH}+r_A+r_{HR-V})-2r_H(r_{VR-T}+r_{VR-ETH}+r_{HR-V}+r_V)}{r_A-r_{VR-T}-r_V-r_H}$	”	
	$R_{511} = \frac{a}{3\sqrt{3}} \frac{(r_{AR-D}+r_{EDA})(r_{VR-ETH}+r_{HR-V})-r_A r_H}{r_{AR-D}+r_{EDA}+r_{VR-ETH}+r_{HR-V}-r_A-r_H}$	$r_{EDA} > r_A$	

TABLE VII
SIMPLIFIED EQUATIONS CORRESPONDING TO TABLE VI AFTER DROPPING RESTRICTION

	$R_{100} = \frac{a}{4}r_D$	
	$R_{110} = \frac{a}{2\sqrt{2}}r_M$	
	$R_{111} = \frac{a}{\sqrt{3}}\frac{r_T r_{L(T)}}{r_T + r_{L(T)}}$	
K_T	$R_{210} = \frac{a}{4\sqrt{5}}(r_M + r_{EMK} + r_K)$	$r_K > r_{EMK}$
	$R_{530} = \frac{a}{2\sqrt{34}}(2r_M + r_{EMK} + r_K)$	,,
K_S	$R_{310} = \frac{a}{2\sqrt{10}}(r_{KR(1)-EMK} + r_K)$	$r_K > r_{KR(1)-EMK}$
	$R_{410} = \frac{a}{4\sqrt{17}}(2r_{KR(1)-EMK} + r_D + 2r_K)$	,,
M_T	$R_{221} = \frac{a}{6}\frac{(2r_T + r_{ETM})(r_M + r_{L(ETM)}) - r_M(r_T + r_{ETM})}{r_T + r_{L(ETM)}}$	$r_{ETM} > r_M$
	$R_{553} = \frac{a}{\sqrt{59}}\frac{(3r_T + r_{ETM})(r_M + r_{L(ETM)}) - r_M(2r_T + r_{ETM})}{r_T + r_{L(ETM)}}$	,,
M_S	$R_{331} = \frac{a}{\sqrt{19}}\frac{(r_T + r_{ETM})(r_M + r_{L(ETM)}) - r_M^2}{r_T + r_{ETM} + r_{L(ETM)} - r_M}$	$r_{ETM} > r_M$
	$R_{441} = \frac{a}{2\sqrt{33}}\frac{(2r_T + r_M + 2r_{ETM})(3r_M + r_{L(ETM)}) - 3r_M(r_T + 2r_M + r_{ETM})}{r_T + r_{ETM} + r_{L(ETM)} - r_M}$	,,
D_T	$R_{211} = \frac{a}{2\sqrt{6}}\frac{r_H(2r_T + r_V)}{r_H + r_T + r_V - r_{ETH}}$	$r_H > r_A$
	$R_{533} = \frac{a}{\sqrt{43}}\frac{r_H(3r_T + r_V)}{r_H + r_T + r_V - r_{ETH}}$	$r_H > r_{ETH}$
D_S	$R_{311} = \frac{a}{\sqrt{11}}\frac{r_H(r_T + r_V)}{r_H + r_T + r_V - r_A}$	$r_H > r_A$
	$R_{411} = \frac{a}{2\sqrt{18}}\frac{r_H(r_{ETH} + r_A + r_V) - 2r_H(r_T + r_{ETH} + 2r_V)}{r_A - r_T - r_V - r_H}$	,,
	$R_{511} = \frac{a}{3\sqrt{3}}\frac{(r_D + r_{EDA})(r_{ETH} + r_V) - r_A r_H}{r_D + r_{EDA} + r_{ETH} + r_V - r_A - r_H}$	$r_{EDA} > r_A$

should be maintained. After all, the restricted sites appear in the equations only because of the initial history of the sites that emerge to the surface, before they become active as an edging species (such as ETH, ETM, EMK, or EDA), a pure step site (such as M, H, V), or a kink site (such as K or A). From this point of view, dropping restriction and keeping edging are justified as a means to reduce the number of different rates. There is only one exception to this rule, namely, the site KR(1)-EMK. It is maintained since it enables fitting the orientations (210) and (310) simultaneously.

Typically, after this simplification, it is only possible to use one orientation from each subfamily in order to carry out the fit due to the similarity between the resulting equations. As an example, we can use the experimental etch rate for (210) or (530), but not both. If we fit, e.g., (210), we can only hope that the calculated/simulated etch rate of (530) will be close to the experimental value, or the other way around. Similarly, in the case of the M_T and M_S subfamilies, only one of the four orientations shown in Table VII can typically be used for the fitting procedure. We have found that this approach is typically acceptable, often involving an error of about 5%, which is normally less. An exception to this case is the D_S subfamily, where both (211) and (311) can be fitted simultaneously.

The fitting procedure typically consists on using the etch rates for nine orientations [e.g., (100), (110), (111), (210), (310), (331), (211), (311), and (511)] in order to obtain values for r_D, r_M, r_T, r_K, r_{EMK}, $r_{KR(1)-EMK}$, r_{ETM}, r_H, r_V, r_{ETH}, r_A, r_{EDA}, and $r_L = r_{L(T)} = r_{L(ETM)}$. This is done as follows.

1) r_D and r_M are obtained trivially from $R_{(100)}$ and $R_{(110)}$, respectively.
2) A value for r_K is chosen so that $r_K > r_D$, and the values for r_{EMK} and $r_{KR(1)-EMK}$ are obtained by solving from the equations for (210) and (310), respectively. Change

r_K if necessary in order to ensure that $r_K > r_{EMK}$ and $r_K > r_{KR(1)-EMK}$.
3) A value is chosen for $r_{L(T)}$ such that $r_{L(T)} > r_K$ and r_T is solved from the equation for (111).
4) Choose $r_{L(ETM)} = r_{L(T)}$ and obtain r_{ETM} from the equation for (331). If $r_{ETM} > r_M$, go to the next item in this list. Otherwise, recalculate r_{ETM} by setting $r_{L(M)} = r_{L(T)}$ and using $R_{(331)} = (a/\sqrt{19})(r_M(2r_T + r_{L(M)}))/(r_T + r_M + r_{L(M)} - r_{ETM}))$. This expression for the etch rate of (331) is obtained from the M_T row of Table V after dropping restriction.
5) Choose values for r_H and r_V such that $r_V > r_H$, and obtain values for r_{ETH}, r_A, and r_{EDA} from the equations for (211), (311), and (511), respectively. We need to ensure that the choice of $r_V > r_H$ produces $r_H > r_A$, $r_H > r_{ETH}$, and $r_{EDA} > r_A$.

B. Results

We have applied the previous fitting scheme to different experimental conditions, including 30%, 40%, and 50% KOH at 70 °C and 20% TMAH at 80 °C using data from previous studies [5], [27]. As an example, Fig. 13 shows a comparison of the simulated and experimental etch rates for orientations in the {110} crystallographic zone. The experimental data correspond to a vertically DRI etched wagon wheel pattern whose wedges are wet-etched in 50% w/v KOH at 70 °C [27]. Each simulation point corresponds to one surface orientation simulated using the CCA method. In this figure, the difference between (a) and (b) underlines the existence of certain flexibility when performing the fitting procedure presented in Section IV-A. In both cases, the specific orientations used for the fit are plotted using triangles, differing only in the choice of one single orientation used for describing the shape of the maximum around {110}. For
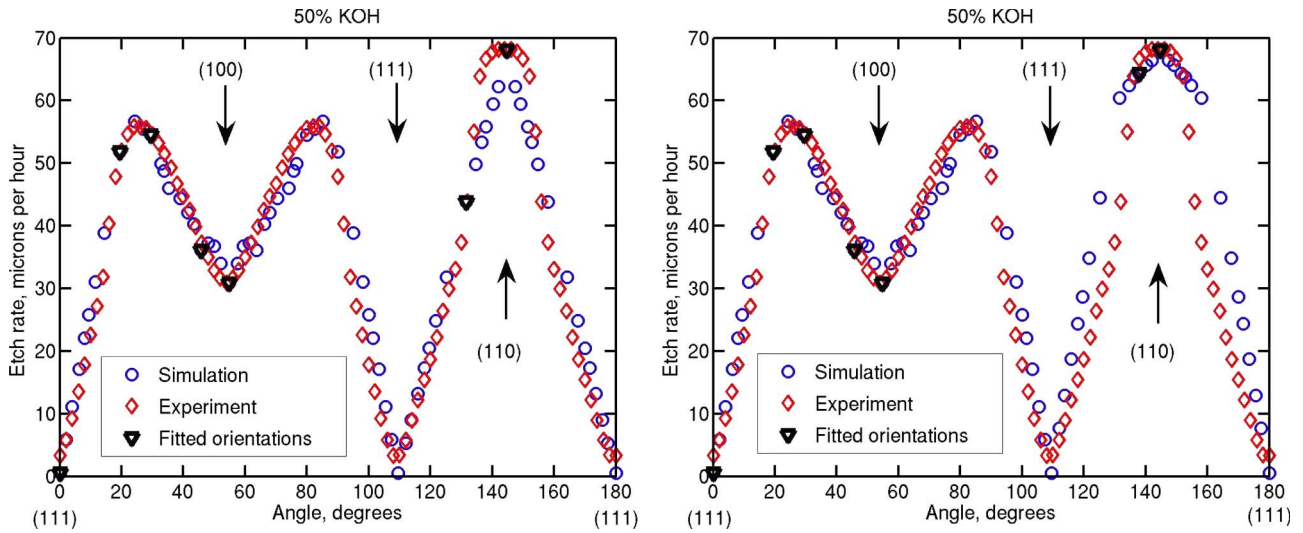
Fig. 13. Comparison of the simulated and experimental etch rates for orientations in the {110} crystallographic zone. (a) and (b) differ in the choice of one orientation for fitting the shape of the maximum around (110). Experimental data from DRI etched wagon wheel anisotropically etched in 50% w/v KOH at 70 °C [27]. Etching is simulated on each orientation separately.
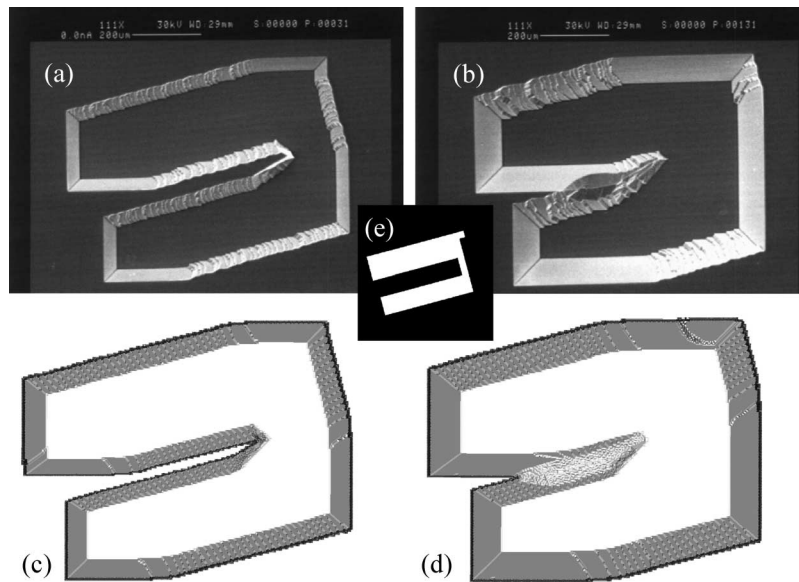

Fig. 14. Comparison of experiment (a)–(b) and simulation (c)–(d) for a misaligned mask pattern, as shown in (e). The simulations assume 30% w/v KOH at 70 °C [27]. Experimental images (30 wt.% KOH at 80 °C) from Collection of Examples, SIMODE: A simulation tool for orientation-dependent etch processes, pp. 33–34, © 2001 Gesselschaft fur Mikroelektronikan-wendung Chemnitz mbH.

case (a), the fitted surfaces are as follows (triangles from left to right): {111}, {211}, {311}, {911}, {100}, {331}, and {110}. Case (b) uses {661} instead of {331}. In both cases, {210} and {310} in the {100} crystallographic zone were also fitted. Case (a) describes step flow around {111} more accurately, and case (b) describes the region of the {110} maximum better. Although none of the two cases provides a perfect match, the overall description of the etch rate anisotropy is good. Further discussion about fitting the shape of the {110} maximum is provided in the Discussion section (Section V).

Beyond the comparison of the etch rates for a multitude of surfaces, Figs. 14–17 show realistic simulations and their comparison to available experiments from the literature. Considering that the etch rates from the studies in [5] and [27] (which we use to fit the removal rates) do not always match

the experimental conditions of the shown experiments, the accuracy of the simulations is very good. The program used for the simulations ("VisualTAPAS") can be freely downloaded from http://www.fyslab.hut.fi/~mag/VisualTAPAS/Home.html.

V. DISCUSSION

The fabrication of MEMS and NEMS devices using bulk and surface micromachining is based on the sequential application of complex process flows involving numerous steps. An efficient design requires the use of realistic and accurate simulations of each individual process. In the previous sections, we have shown that it is possible to solve analytically the time evolution of the CCA method, making it particularly suitable for the realization of realistic simulations of anisotropic
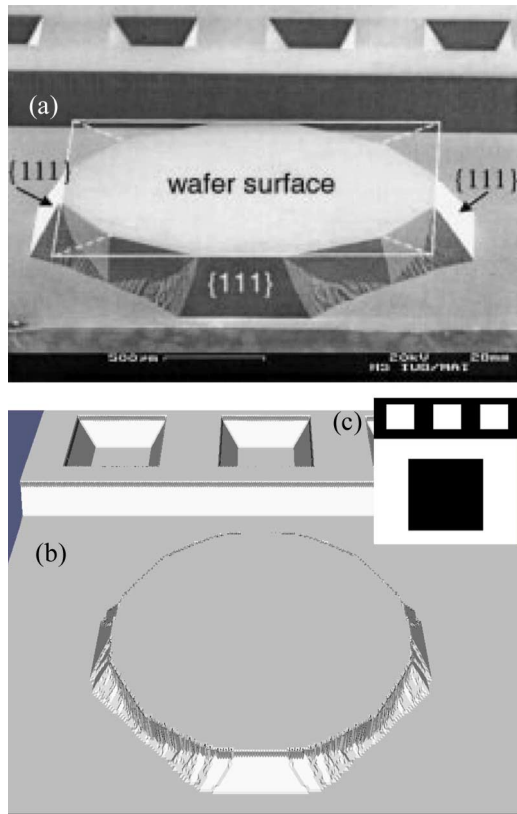
Fig. 15.   Convex corner undercutting simulated for 30% w/v KOH at 70 °C. Experimental image from [28] corresponds to 33 wt.% KOH at 80 °C. Reproduced with permission (© IEEE 2001).
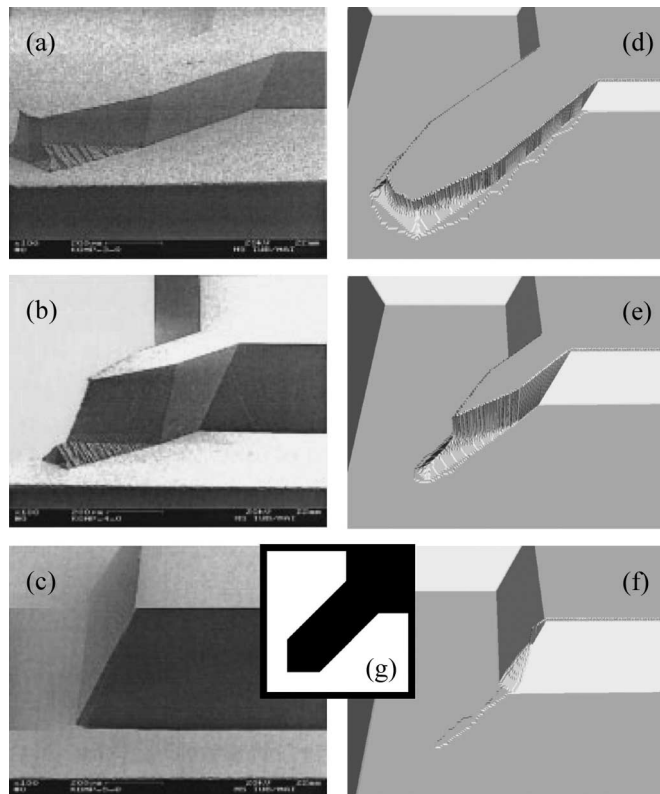

Fig. 16.   Convex corner compensation simulated for 30% w/v KOH at 70 °C. Experimental images from [28] correspond to 33 wt.% KOH at 80 °C. Reproduced with permission (© IEEE 2001).

etching. In particular, Sections II and III have presented a theoretical description of the orientation dependence of the etch rate in terms of the most active atomistic removal rates based on the fulfillment of step propagation on each family of surface orientations. In Section IV, we have shown that the approach is both flexible and accurate for the simulation of anisotropic etching for engineering applications. As compared to the geometrical methods, our approach allows a reduction in the number of input experimental etch rates that is necessary for simulating etching. The number of rates is reduced from hundreds or even thousands to just a few, typically nine.

Although the step-flow aspects of anisotropic etching have been taken into account in earlier simulation approaches, particularly through the use of MC methods [7], [8], [10], we are not aware of any report of a CA method explicitly built upon step propagation. Schröder *et al.* [28] and Horn *et al.* [29] have proposed a step-flow model for explaining the various shapes of convex corner underetching. However, their approach does not fall into the CA category of methods, and it does not provide an analytical solution either. Originally, they used structuring elements, an idea borrowed from image processing. Later on, they used the actual equations of motion for the propagation of the cells on the etch front, explicitly incorporating some aspects from step flow.

Similarly, we are not aware of any successful attempt previous to the present study to solve analytically the expression of the etch rate as a function of the removal rates of the active atoms in a CA simulation of anisotropic etching. The closest study is by Zhou *et al.* [19], although they assumed that the etch rate for each surface orientation is essentially determined by one single atom species. More recently, they have explored a labor-intensive fitting procedure leading to numerical expressions for the etch rates [20]. By determining in this paper the actual expressions which link the etch rates of the surfaces to the atomistic removal rates of the surface atoms, a completely unforeseen level of complication in the dependence has been uncovered. This is very surprising, particularly when one considers the simplicity of the step-flow process realized on each orientation.

The success of this paper relies significantly on Zhou's indexing scheme [19], [20] and on our step-flow-based classification of the surface sites. During a simulation, the indexing scheme allows one to identify the type of a surface atom according to Table III and, as a result, to associate a removal rate to it.

The geometrical analysis presented in Section II is very similar in spirit to that by Zubel [37], [38]. However, we focus on the characterization of the surface sites according to the step-flow nature of etching instead of on a purely geometrical classification of the surface bond types. The geometrical features of the two approaches can probably be mapped, if not quantitatively, at least qualitatively. For instance, we may regard the classification of the surface bonds as an alternative to the classification of the surface sites according to the four indices by Zhou *et al.* [19], [20]. However, we go beyond these geometrical aspects and incorporate the important role of step flow, solving eventually the dependence of the etch rate for the different surface families. Although Zubel's approach is potentially capable of simulating etching in arbitrary geometries
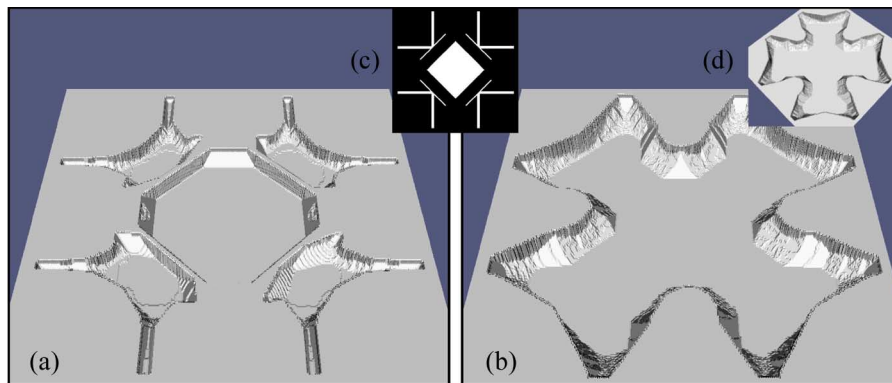
Fig. 17.   (a), (b) Two time shots of a simulation of anisotropic etching. The mask used is shown in (c). A top view of the final result, which resembles the German Iron Cross, is shown in (d). This image is rotated 45° with respect to (b). The simulation corresponds to 40% w/v KOH at 70 °C [27].

for engineering purposes, just in the same manner as Zhou's indexing scheme allows this type of simulations, the method has not been used in that context. Zubel's classification of the bonds seems to consider a subset of the surface sites included in our analysis (Figs. 6 and 7), which describes a larger neighborhood of the target atoms.

Wind *et al.* [27] have used a simple step-flow model to describe the anisotropy of the etch rate in the vicinity of {111}. The model is a purely theoretical description based on an orientation-independent step velocity (v_{step}) and an orientation-dependent step density ($\sin \theta$). In particular, it is not intended for simulating etching. As for the case of our CA, the model describes the overall mean-field propagation of the steps, disregarding some details of the process, such as the sequential nature of etching, involving fast etching of step sites, fast etching of kink sites, or a combination of both. Although none of the two models incorporates explicitly the fine details of diffusion transport, they may be considered to contain implicitly diffusion effects in the form of step bunching [10], [11]. In our CA, the sequential events and details of the propagation of a step are substituted by the removal of all the atoms appearing at the step (in parallel, not sequentially) according to a suitable average removal rate. Although Wind *et al.* do not consider it, one can associate this rate to the propagation of the step bunches instead of the atomistic steps, thus regarding v_{step} as the velocity of the bunches. Since the propagation is typically modeled as the removal of generic P and Q atom rows (Section III-A), the average step velocity v_{step} is "split" into the step velocities (or removal rates) of the two atom species, representing the motion of the step bunches. Due to the continuous values of the occupation used for the CCA implementation, the removal rates of various terrace sites appear in the final expressions for the etch rates of the surfaces together with geometrical factors in a manner that is similar to—but much more complicated than—the $\sin \theta$ factor. Although Wind *et al.* are very critical in their analysis, concluding that a step-density-independent step velocity is inconsistent with the formation of step bunches on these surfaces, we find no conceptual problem since their v_{step} and the removal rates in our model represent already averaged quantities. Although the formation of step bunches actually requires step-density-dependent single-step velocities, as shown in [8] and [10], the resulting velocity of the step

bunches can be effectively independent of the step density for a certain range of orientations.

Considering the previous paragraph, it is not surprising that our step-flow model provides an accurate description of the etch anisotropy in the vicinity of {111} [see, e.g., Fig. 13(a)]. However, we also describe etching as a step-flow process around {100} and {110}. This appears to be suitable for {100}, but it seems to be inaccurate for {110} [see Fig. 13(a) and (b)]. From the zigzag surface morphology of {110} [10], [11], it is known that this surface and its vicinal orientations are etched essentially as a step-flow process occurring parallel to the facets of the zigzag structures and not parallel to the {110} plane, as modeled in our analytical solutions. This particular zigzag morphology is probably the result of transport diffusion delay [10]. According to Wind *et al.* [27], the isotropy of the etch rate around {110} can be explained due to the particular features of this morphology. This means that a better description of the etching process for these surfaces can be obtained by considering an alternative etching mode producing zigzags instead of smooth stepped surfaces during the analytical analysis. This will be the subject of further research in the near future.

A more sophisticated approach for the description of the etch rate anisotropy around any surface orientation has been presented by van Veenendaal *et al.* [26], [39] and Nguyen and Elwenspoek [40]. The method, which is not meant for simulations either, is used for the analysis of the etch rate anisotropy, providing a deeper understanding of the relative importance of different processes in shaping the anisotropy. The processes that are considered include step flow and pit nucleation (roughening) as well as effects from step bunching and other mesoscopic instabilities. As for Wind's case and our approach, their analysis corresponds to a mean-field picture of etching. As in our case, the accurate description of the fine details of the etch rate around {110} is also a challenge in their approach.

The integral form in (3) has been presented as the fundamental principle of the CCA method. It is a statement of the relation between the occupation of the sites (or cells) and the atomistic (or process) rates. We are not aware of any previous study establishing such a relation. Our derivations can be seen as an example of the use of the CCA in order to simulate the evolution of an interface and, simultaneously, to solve it analytically. In principle, the same expression can be applied

also to other interface propagation problems for other systems. As in our case, (3) can probably be used for the derivation of implicit and/or explicit equations relating the time increments of the evolution and the process rates of specific types of cells. The fact that step flow has been incorporated in the analysis due to the particular nature of the etching process has facilitated the derivation of analytical expressions. For more general interface propagation problems, the analytical description may become very sophisticated.

The useful property of the CCA is that it can describe the average propagation of the surface with the correct overall etch rate by actually using a propagation mode that differs from the experiment. As an example, for {111}, the CCA removes the terrace atoms T very slowly and then the lollies L(T) very fast. Except for a geometrical factor, the overall etch rate for the plane is $R_{111} = r_T r_{L(T)}/(r_T + r_{L(T)})$. By choosing r_T and $r_{L(T)}$, any etch rate for R_{111} can be described. Although this represents the global etch rate correctly, etching is effectively simulated as a gradual motion of the interface due to the slow removal of the T atoms and a sudden jump in the propagation due to the removal of the L(T) atoms. This occurs when $r_{L(T)} = 1$, which is a valid choice. Although a more gradual motion can be achieved using a smaller $r_{L(T)}$, the simulations will still proceed differently from the experiment, where a few pits are nucleated by the removal of a few T atoms, giving way to the formation of steps at the pit boundaries and, thus, step flow. As the pit boundaries grow, a layer is eventually removed. Thus, the CCA method provides a mean-field propagation mode that reproduces the overall propagation rate even though each layer is removed in a manner that differs from the experiment.

Note that, in the event that a pit is formed on {111}, step flow of the pit boundaries will occur in the CCA simulation. In this case, the velocity of step flow is fixed by the overall propagation of surface orientations containing solely these steps (and terraces between them). In the same way, steps can be induced due to the masking pattern, e.g., at the convex corners. In addition to matching the overall etch rates of the planes, these atomistic features make the simulations very realistic. For {110}, whose etch rate can be described correctly by simply removing layers of M atoms, the etching mode strongly differs from the experiment, where typically the zigzag structures are formed. As mentioned previously, the CCA etch rates for vicinal orientations of {110} differ from the experiment because the etching mode using zigzags structures is not considered. As for the case of pits, should kinks be introduced in the steps, the CCA simulation will proceed by propagating the kinks. In this manner, the basic atomistic features are reproduced, but the particular rates correspond to the overall mean-field behavior and not necessarily to the corresponding atomistic process.

At the global scale, the obtained removal rates provide a rather accurate fit for the etch rates of the different orientations. At the microscopic scale, the parameters describe step flow, including the propagation of pit boundaries. We cannot claim, however, that the atomistic rates for the step sites are suitable for atomistc simulations, such as kinetic MC simulations. Indeed, they are not suitable. The reason for this is that the removal rates for the step sites are obtained by considering the gradual removal of the complete step simultaneously, not as a result of kink propagation. Thus, these rates fulfill the average propagation of the step in the same way as r_T and $r_{L(T)}$ fulfill the overall etch rate of {111}, but not necessarily with the correct atomistic values.

VI. CONCLUSION

This paper shows how to solve analytically the time evolution of the CCA method for the simulation of anisotropic etching for use in the fabrication of MEMS/NEMS. By presenting a wide collection of generic examples, we show that the etch rate of any surface orientation can be obtained from the geometrical and kinetic analyses of the mean-field picture of the step-flow process underlying etching. This requires a purely geometrical determination of the changes in the average height of the system and a purely kinetic description of the site-type histories of the removed atoms. Depending on the specific values of the removal rates of the step atoms, different realizations of step flow are obtained, and correspondingly, different expressions for the etch rates of the different surfaces are derived. An important physical input for the derivation is the step-flow nature of the process, a feature that lies at the root of the nomenclature introduced for classifying the surface sites.

As a result of the existence of analytical expressions for the etch rates of the crystallographic planes as a function of the removal rates of the active atoms, we show that it is possible to fit the removal rates using the etch rates of a small set of surface orientations such as, e.g., (100), (110), (111), (210), (310), (331), (211), (311), and (911). As compared to the geometrical methods, our approach allows a significant reduction in the number of input experimental etch rates, decreasing the number to only a few instead of hundreds or thousands of orientations. We provide the guidelines of the fitting process, which can be automated, and the results of the simulations are compared satisfactorily with the experiments. As a result of the study, a freely available simulator of anisotropic and dry etching known as VisualTAPAS has been developed (http://www.fyslab.hut.fi/~mag/VisualTAPAS/Home.html).

REFERENCES

[1] J. Frühauf, K. Trautman, J. Wittig, and D. Zielke, "A simulation tool for orientation dependent etching," *J. Micromech. Microeng.*, vol. 3, no. 3, pp. 113–115, 1993.
[2] C. H. Sequin, "Computer simulation of anisotropic crystal etching," *Sens. Actuators A, Phys.*, vol. 34, no. 3, pp. 225–241, Sep. 1992.
[3] G. Li, T. Hubbard, and E. K. Antonsson, "SEGS: On-line WWW etch simulator," in *Proc. Int. Conf. MSM*, Santa Clara, CA, Apr. 6–8, 1998, pp. 356–361.
[4] K. Asaumi, Y. Iriye, and K. Sato, "Anisotropic-etching process simulation system MICROCAD analyzing complete 3D etching profiles of single crystal silicon," in *Proc. IEEE Int. Conf. MEMS*, Nagoya, Japan, Jan. 26–30, 1997, pp. 412–417.
[5] K. Sato, M. Shikida, Y. Matsushima, T. Yamashiro, K. Asaumi, Y. Iriye, and M. Yamamoto, "Characterization of orientation-dependent etching

properties of single-crystal silicon: Effects of KOH concentration," *Sens. Actuators A, Phys.*, vol. 64, no. 1, pp. 87–93, Jan. 1998.

[6] *FabMeister-ES Etching Simulator With Embedded Database (Formerly MICROCAD)*. [Online]. Available: http://www.mizuho-ir.co.jp/english/solution/microcad/index.html

[7] J. Flidr, Y. C. Huang, T. A. Newton, and M. A. Hines, "An atomistic mechanism for the production of two- and three-dimensional etch hillocks on Si(111) surfaces," *J. Chem. Phys.*, vol. 111, no. 15, pp. 5542–5553, 1998.

[8] S. P. Garcia, H. Bao, and M. A. Hines, "Etchant anisotropy controls the step bunching instability in KOH etching of silicon," *Phys. Rev. Lett.*, vol. 93, no. 16, p. 166 102, Oct. 2004.

[9] M. Gosálvez and R. M. Nieminen, "Surface morphology during anisotropic wet chemical etching of crystalline silicon," *New J. Phys.*, vol. 5, p. 100, 2003.

[10] M. Gosálvez, Y. Xing, T. Hynninen, M. Uwaha, A. S. Foster, R. M. Nieminen, and K. Sato, "Faster simulations of step bunching during anisotropic etching: Formation of zigzag structures on Si(110)," *J. Micromech. Microeng.*, vol. 17, no. 4, pp. S27–S37, Apr. 2007.

[11] M. Gosálvez, K. Sato, A. S. Foster, R. M. Nieminen, and H. Tanaka, "An atomistic introduction to anisotropic etching," *J. Micromech. Microeng.*, vol. 17, no. 4, pp. S1–S26, Apr. 2007.

[12] M. Gosálvez, P. Kilpinen, E. Haimi, R. M. Nieminen, and V. Lindroos, "Anisotropic wet chemical etching of crystalline silicon: Atomistic Monte-Carlo simulations and experiments," *Appl. Surf. Sci.*, vol. 178, no. 1–4, pp. 7–26, Jul. 2001.

[13] M. Gosálvez, A. S. Foster, and R. M. Nieminen, "Atomistic simulations of surface coverage effects in anisotropic wet chemical etching of crystalline silicon," *Appl. Surf. Sci.*, vol. 202, no. 3/4, pp. 160–182, Dec. 2002.

[14] Z. Zhu and C. Liu, "Simulation of anisotropic crystalline etching using a continuous cellular automata algorithm," *Comput. Model. Eng. Sci.*, vol. 1, no. 1, pp. 11–19, 2000.

[15] Z. Zhu and C. Liu, "Micromachining process simulation using a continuous cellular automata method," *J. Microelectromech. Syst.*, vol. 9, no. 2, pp. 252–261, Jun. 2000.

[16] Z.-F. Zhou, Q.-A. Huang, W.-H. Li, and C. Zhu, "A 3-D simulator for silicon anisotropic wet chemical etching process based on cellular automata," *J. Phys., Conf. Series*, vol. 34, pp. 674–679, 2006.

[17] O. Tan and S. Büttgenbach, "Simulation of anisotropic chemical etching of crystalline silicon using a cellular automata model," *Sens. Actuators A, Phys.*, vol. 45, no. 1, pp. 85–89, Oct. 1994.

[18] S. Büttgenbach and O. Tan, "SUZANA: A 3D CAD tool for anisotropically etched silicon microstructures," in *Proc. IEEE ED TC*, 1996, pp. 454–458.

[19] Z. F. Zhou, Q. A. Huang, W. H. Li, and W. Deng, "A three-dimensional continuous cellular automata model for silicon wet chemical anisotropic etching simulation," in *Proc. 5th Int. Workshop PCWES*, Saarbrucken, Germany, Jun. 19–21, 2006, p. 59.

[20] Z. F. Zhou, Q. A. Huang, W. H. Li, and W. Deng, "A cellular automaton-based simulator for silicon anisotropic etching processes considering high index planes," *J. Micromech. Microeng.*, vol. 17, no. 4, pp. S38–S49, Apr. 2007.

[21] P. Allongue, H. Brune, and H. Gerischer, "In situ STM observations of the etching of n-Si(111) in NaOH solutions," *Surf. Sci.*, vol. 275, no. 3, pp. 414–423, 1992.

[22] M. Elwenspoek, "On the mechanism of anisotropic etching of silicon," *J. Electrochem. Soc.*, vol. 140, no. 7, pp. 2075–2080, Jul. 1993.

[23] P. Allongue, V. Costa-Kieling, and H. Gerischer, "Etching of silicon in NaOH solutions: I. In situ scanning tunneling microscopic investigation of n-Si(111)," *J. Electrochem. Soc.*, vol. 140, no. 4, pp. 1009–1018, Apr. 1993.

[24] M. A. Hines, Y. J. Chabal, T. D. Harris, and A. L. Harris, "Measuring the structure of etched silicon surfaces with Raman spectroscopy," *J. Chem. Phys.*, vol. 101, no. 9, pp. 8055–8072, 1994.

[25] J. Kasparian, M. Elwenspoek, and P. Allongue, "Digital computation and in situ STM approach of silicon anisotropic etching," *Surf. Sci.*, vol. 388, no. 1, pp. 50–62, Oct. 1997.

[26] E. van Veenendaal, A. J. Nijdam, J. van Suchtelen, K. Sato, J. G. E. Gardeniers, W. J. P. van Enckevort, and M. Elwenspoek, "Simulation of anisotropic wet chemical etching using a physical model," *Sens. Actuators A, Phys.*, vol. 84, no. 3, pp. 324–329, Sep. 2000.

[27] R. A. Wind, H. Jones, M. J. Little, and M. A. Hines, "Orientation-resolved chemical kinetics: Using microfabrication to unravel the complicated chemistry of KOH/Si etching," *J. Phys. Chem., B*, vol. 106, no. 7, pp. 1557–1569, 2002.

[28] H. Schröder, E. Obermeier, A. Horn, and G. K. M. Wachutka, "Convex corner undercutting of 100 silicon in anisotropic KOH etching: The new step-flow model of 3-D structuring and first simulation results," *J. Microelectromech. Syst.*, vol. 10, no. 1, pp. 88–97, Mar. 2001.

[29] A. Horn, H. Schroeder, E. Obermeier, and G. Wachutka, "Simulation of orientation-dependent etching of silicon using a new step flow model of 3D structuring," in *Sonderforschungsbereich 438*. TU-München: Universität Augsburg, 2000. Preprint SFB-438-0010.

[30] H. Camon, A. M. Gue, J. S. Danel, and M. Djafari-Rouhani, "Modelling of anisotropic etching in silicon-based sensor application," *Sens. Actuators A, Phys.*, vol. 33, no. 1/2, pp. 103–105, May 1992.

[31] H. Camon and Z. Moktadir, "Atomic scale simulation of silicon etched in aqueous KOH solution," *Sens. Actuators A, Phys.*, vol. 46, no. 1–3, pp. 27–29, Jan.–May 1995.

[32] H. Camon, Z. Moktadir, and M. Djafari-Rouhani, "New trends in atomic scale simulation of wet chemical etching of silicon with KOH," *Mater. Sci. Eng. B*, vol. 37, no. 1, pp. 142–145, Feb. 1996.

[33] H. Camon and Z. Moktadir, "Simulation of silicon etching with KOH," *Microelectron. J.*, vol. 28, pp. 509–517, 1997.

[34] The Simulator Has Been Developed in Nagoya University. The web page is maintained by the first author, now at HUT. [Online]. Available: http://www.fyslab.hut.fi/~mag/VisualTAPAS/Home.html

[35] E. Kita and T. Toyoda, "Structural design using cellular automata," *Struct. Multidisc. Optim.*, vol. 19, no. 1, pp. 64–73, Mar. 2000.

[36] P. Hajela and B. Kim, "On the use of energy minimization for CA based analysis in elasticity," *Struct. Multidiscpl. Optim.*, vol. 23, no. 1, pp. 24–33, 2001.

[37] I. Zubel, "The influence of atomic configuration of (h k l) planes on adsorption processes associated with anisotropic etching of silicon," *Sens. Actuators A, Phys.*, vol. 94, no. 1, pp. 76–86, Oct. 2001.

[38] I. Zubel and M. Kramkowska, "Etch rates and morphology of silicon (h k l) surfaces etched in KOH and KOH saturated with isopropanol solutions," *Sens. Actuators A, Phys.*, vol. 115, no. 2/3, pp. 549–556, Sep. 2004.

[39] E. van Veenendaal, J. van Suchtelen, W. J. P. van Enckevort, K. Sato, A. J. Nijdam, J. G. E. Gardeniers, and M. Elwenspoek, "The construction of orientation-dependent crystal growth and etch rate functions II: Application to wet chemical etching of silicon in potassium hydroxide," *J. Appl. Phys.*, vol. 87, no. 12, pp. 8732–8740, Jun. 2000.

[40] Q. D. Nguyen and M. Elwenspoek, "Characterisation of anisotropic etching in KOH using network etch rate function model: Influence of an applied potential in terms of microscopic properties," *J. Phys., Conf. Series*, vol. 34, pp. 1038–1043, 2006.

Miguel A. Gosálvez received the M.S. degree (licentiate) in materials physics from the Universidad Complutense de Madrid, Madrid, Spain, in 1996, and the Ph.D. degree in computational physics from Helsinki University of Technology, Espoo, Finland, in 2003.

He was a COE Research Scientist from April 2004 to March 2006 and an Assistant Professor from April 2006 to March 2007 in the Sato Laboratory, Department of Micro-Nano Systems Engineering, Nagoya University, Nagoya, Japan. Currently, he is with the Laboratory of Physics, Helsinki University of Technology. His research focuses on the simulation of surface processes such as anisotropic etching and reactive ion etching using kinetic Monte Carlo and cellular automata methods aiming at the fundamental understanding of the processes and enabling practical simulations for engineering applications.

Yan Xing received the B.S., M.S., and Ph.D. degrees in mechanical engineering from Southeast University, Nanjing, China, in 1993, 1996, and 2001, respectively.

He was with the Department of Micro-Nano Systems Engineering, Nagoya University, Nagoya, Japan. He is currently an Associate Professor with the Department of Mechanical Engineering, Southeast University, Nanjing, China. He has been studying numerical simulation technologies with respect to MEMS CAD, semiconductor processes, and integrated information systems in automation.

Kazuo Sato received the B.S. degree in mechanical engineering from Yokohama National University, Yokohama, Japan, in 1970, and the Ph.D. degree from the University of Tokyo, Tokyo, Japan, in 1982.

He was with Hitachi Ltd. from 1970 to 1994. He has been a Professor with the Micromachining and MEMS Laboratory, Department of Micro-Nano Systems Engineering, Nagoya University, Nagoya, Japan, since 1994. He started MEMS research in 1983. His research interests include chemical anisotropic etching, characterization of MEMS materials, microsensors, microactuators, and micro/nanophysics.

Dr. Sato is a Fellow and a Board Member of the Japan Society of Mechanical Engineers, a Senior Member of the Institution of Electrical Engineers, and a Board Member of the Japan Society for Precision Engineering. He was a cochair of the 1997 IEEE MEMS Workshop.